Escuela de Caminos
Escuela Técnica Superior de Ingenieros de Caminos, Canales y Puertos
UPC BARCELONATECH

TRABAJO FINAL DE MASTER

Numerical Simulation of AM processes by SLM technology

Trabajo realizado por:
Reinaldo Wiener Rocca

Dirigido por:
Michele Chiumenti

Máster en:
Métodos Numéricos en Ingeniería

Barcelona, 28 de Septiembre de 2018

Departamento de Ingeniería Civil y Ambiental

Table of Contents

1. Introduction

Additive manufacturing (AM) or 3D printing is a process in which 3D physical objects are built by adding layers to a base material, following a path defined by a 3D digital model. The first 3D printer was invented and patented in 1983 by Charles Hull, an American inventor. After the invention, this technology was a breakthrough in the industry at the time but after 2010 it has been more known among the general masses. Comparing to other manufacturing processes the big advantage of the AM is the degree of freedom in the parts design. For example restrictions like: tooling access, tooling space, tooling angles, de-molding angles; are not present in AM. This opens the door to the manufacture of highly complex and custom geometries, which can still be extremely light and strong. The offer of materials is becoming larger each day, offering a variety of options for the family.

Figure 1 shows an example of the level of complexity that can be achieved. This object was built using Selective Laser Melting (SLM), which is one of the AM technologies. As it can be seen, this part is not only small (around 3mm per side) but has a complex internal structure, which would be impossible to build using neither machining process nor forging/casting. These kinds of structures are commonly used to optimize weight of prosthetics.

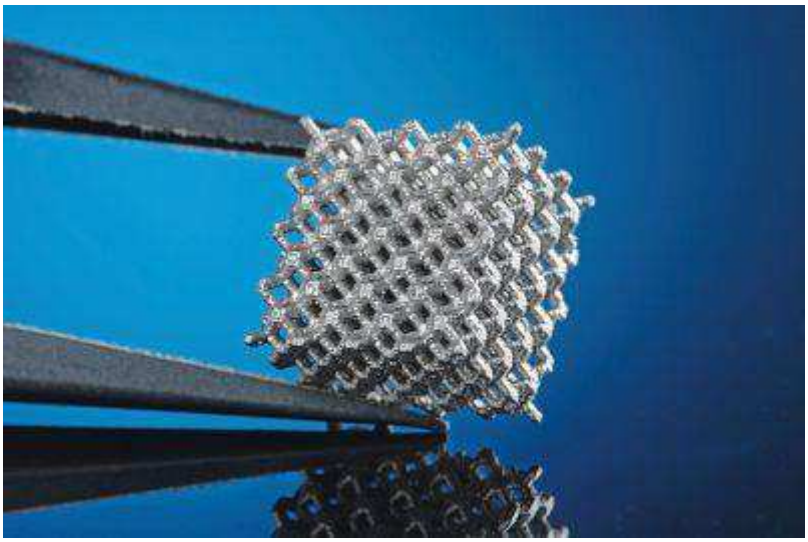

Figure 1: cellular cube built with SLM. Image downloaded from https://www.industrial-lasers.com/articles/2016/03/selective-laser-melting-method-works-with-magnesium-alloys.html.

Another advantage of AM is the reduction of material waste, since the parts are built using the minimum required, in contrast with subtractive manufacturing techniques (milling, lathing, CNC, etc), where material must be removed from an initial raw block. This represents a big advantage in terms of waste lost.

Also for AM the cost of building 1 part or 1 million is the same, which is an advantage for prototyping and designing personalized objects. Although this can be seen as a drawback in terms of mass-production, this is in fact a breakthrough in biomechanical/orthopedics and odontology fields, since with AM is possible to create personalized prosthetics to each patient, without the need to install a whole production line.

Also, top companies like GE and Siemens are betting for this kind of technology to build parts for the aeronautics industry, especially from metal. GE has invested more than $1.5 billion in additive manufacturing technologies so far for their Global Research Center and it is one of the companies that sees the potential of AM. Also Siemens has opened a $23.8-million additive manufacturing production facility for metal parts in Sweden in February 2018, and has recently invested in other AM facility worth in $50-million in the UK. The company is also producing 3D-printed burner component for its heavy-duty gas turbine that is operating at a power plant in the Czech Republic. Other companies like SpaceX and Tesla have also shown their interest for the Aerospace and Automotive applications also.

After this overview of additive manufacturing, a key characteristic of AM will be explained and then the different technologies and materials used will be exposed.

1.1. Support material

One particular characteristic of the AM is the use of support structures. A support structures is added material that acts as support of the final part to avoid large deformations due to residual stresses of body loads during solidification. This structure is thin and is normally from the same material of the main part. After the part is finished these structures are removed using manual processes.

However there are machines that are able to print 2 or more material. For example, Figure 2 shows a part printed using a Fused Deposition Machine with 2 extruders, to be able to print soluble (white) and non-soluble (gray) material. The finished part looks like the right object and after it submerged into a solution that dissolve the support structure it ends like the left object.

Figure 2: 3d printed part with support structure (white). Left: final part, Right: part with support structure. Image downloaded from https://3dfabprint.com/polymakers-new-3d-printing-support-material-polysupport/

This represents in some cases a limitation in the design, but there are practices to minimize the need of support, for example the same part can be rotated to find the position where less support is needed. However, it must be taken into account that there are AM technologies which doesn't require support material, for example the Powder Bed Fusion technologies.

1.2. Materials and technologies

Despite thermoplastics and metals have caught a lot of attention during the boom of 3D printing in the last decade, there are other materials used in AM; like for example ceramics, glass, composites, graphene-embedded plastics, paper, concrete, food, yarn and even bio-inks. Depending of the material required, dimensional accuracy, surface finish specification, post-processing requirements and manufacturing time; a suitable technology must be selected. In the next part, the most common AM technologies are presented to give an idea of the current market status.

1.2.1. Vat Photopolymerization

This method uses as base material a photopolymer resin which change of matter state when is exposed to light at a specific wavelength. To build the part, the material is initially in liquid form and when exposed to light, it solidifies following the cross section pattern of the corresponding layer. This process is repeated layer by layer until the part is completed. Specific technologies that use this method are: Stereolithography (SLA), Direct Light Processing (DLP) and Continuous DLP (CDLP). The main material used is photopolymer resin although ceramic paste consisting of a photopolymer mixed with ceramic powder has also been used to create porcelain objects.

This technology is normally used to manufacture patterns for injection molding, thermoforming and other casting processes, due to the good surface finish and geometrical accuracy. It has also applications in jewelry, dental and medical applications. For example, Figure 3 shows a dental mold build using SLA process to appreciate the quality of the surface finish.

Figure 3: dental mold built using SLA technology. Image downloaded from http://www.methodsmachine.com/assets/SLA_Dental_Mold-577x433.jpg

Main advantage of this technology is the fast processing time, which makes it suitable for prototypes production. However, it also has some drawbacks because it is limited to resins that are cost-expensive and limited in availability; it requires support structure and produced parts are normally brittle.

1.2.2. Material Extrusion

This technology is also known as Fused Deposition Modeling (FDM) and with this method the material is extruded in liquid or viscous state through a nozzle onto a build plate, depositing the material layer by layer. The nozzle follows a predetermined path defined by a 3D design, creating the cross section of each layer. The process is repeated until the part is finished. The most commonly used materials are polymers like ABS, PLA, Nylon, PC, fiber-reinforced Nylon, ULTEM and reinforced filaments (wood-filled, metal-filled, etc). Normally the parts required a post-process work to improve surface finish.

The main advantage of this technology is the quick and cost-effective way of producing plastic prototypes, from different variety of polymers. Figure 4 is an example of an industrial application of FDM, where advance material like ULTEM 9085 is used. This part was built by the NASA for a satellite antenna. The material used is capable of withstand extreme temperatures, vibration, and exposure in outer space. However, in some cases, FDM can manifest dimensional inaccuracy and anisotropic behavior (low resistance in build direction) depending of the selected materials and parameters.

Figure 4: component for a satellite antenna array, built by Fused Deposition Modeling (FDM) and using ULTEM 9085 as material. Image downloaded from: https://www.stratasysdirect.com/resources/case-studies/3d-printed-satellite-exterior-nasa-jet-propulsion-laboratory

1.2.3. Material Jetting

This technology is analogous to the conventional 2D ink jetting process but adding one more dimension. By this method, a photopolymer is injected through hundreds of tiny nozzles onto a base plate and then it is exposed to UV light for solidification. The main advantage of this technology is the velocity to build parts because material deposition is done in a line-wise fashion way instead of following a point-wise path. It is said that this technology is x10 faster than a FDM or Selective Laser Sintering technology.

Due to the number of nozzles it is possible to print different materials at the same time, for example soluble and non-soluble material, what makes it easier to remove the support structures. Material jetting is ideal to build realistic prototypes, showing perfect details, high accuracy, and smooth surface finish and a good example are the helmets of Figure 5. It allows a designer to print in multiple colors in parallel, a characteristic that is not commonly available in all other technologies. Other similar technologies are: Nano particle jetting, where is possible to print metal; and Drop-On-Demand (DOD).

The main drawbacks of material jetting technologies are the high cost and the brittle mechanical properties of the UV activated photopolymers.

Figure 5: Helmets built using material jetting. Image downloaded from: https://www.rnd-tech.com/3d-printing-materials

1.2.4. Binder Jetting

In this process a binding agent is dispensed onto a powder bed to build a part one layer at a time. The particles and the layers bind to one another to form a solid component. This technology is very similar to a power bed fusion but instead of applying an energy source, a binding adhesive is applied to each layer.

One common application is with ceramic-based materials, which are suitable for applications where aesthetics and form are important; like for architectural models, packaging, ergonomic verification, etc. However it is not suitable for functional prototypes, as the parts are very fragile. Ceramic-based Binder Jetting can also be used to create molds for sand casting.

For metals, binder jetting parts are the fastest and cheapest AM technology. It adapts perfectly for prototypes, ornamental/decorative objects and jewelry. Figure 6 shows jewelry built with this process, where it can be seen the quality of the surface finish and accuracy. It can be used also as functional components, but it must be considered that mechanical properties are poorer when comparing to Powder Bed Fusion technologies.

Commonly used material are: ceramics, silica sand, PMMA particle material, gypsum, Stainless steel , cobalt-chrome, tungsten-carbide.

Figure 6: Ornamental accessories using binder jetting. Image downloaded from https://www.sculpteo.com/es/materiales/materiales-binder-jetting/

Some drawbacks are that: post-processing operations are required, furnace heating is required to eliminate the binder, sintered part is porous, mechanical strength is low and there is a limited choice of materials.

1.2.5. Direct Energy Deposition (DED)

Similarly as in the metal inert gas (MIG) welding technology, this method creates parts by melting powder or wired material as it is deposited, following a desired path. It is used exclusively in metal additive manufacturing and it is often referred to as metal deposition. The common technologies used for DED are: Laser Engineered Net Shape (LENS), Electron Beam Additive Manufacture (EBAM).

In LENS technology, a laser beam melts the metal particles, which are blown by nozzles, onto a substrate base plate. This is why this technology is also known as Blown Powder. Inert gas is also blown to isolate the welding pool to avoid oxidation. Common used materials are: titanium, stainless steel, aluminum, copper, tool steel. This technology allows for powder deposition of dimensions of the order of 100μm, making possible to manufacture larger parts faster by using coarser metal powders.

EBAM technology is very similar to LENS but using an electron beam instead of a laser beam. Either metal powder or wire is used to create metal parts. Common materials are: Titanium, stainless steel, aluminum, copper nickel, 4340 steel. This technology allows the metal deposition of 1mm, making possible to manufacture larger parts even faster than using LENS.

Despite the nature of the process is suited for repairing or adding material to existing components, this technology is also used also to build parts. The advantages of this

technology are that the layer can be fabricated in any orientation, a variety of materials can be processed, large components can be manufactured at higher deposition rates.

Some drawbacks of this technology are the lower geometrical accuracy and stair-stepping effect which are clearly seen in Figure 7. It can be seen that finished surface is not smooth, as consequence of the layer thickness.

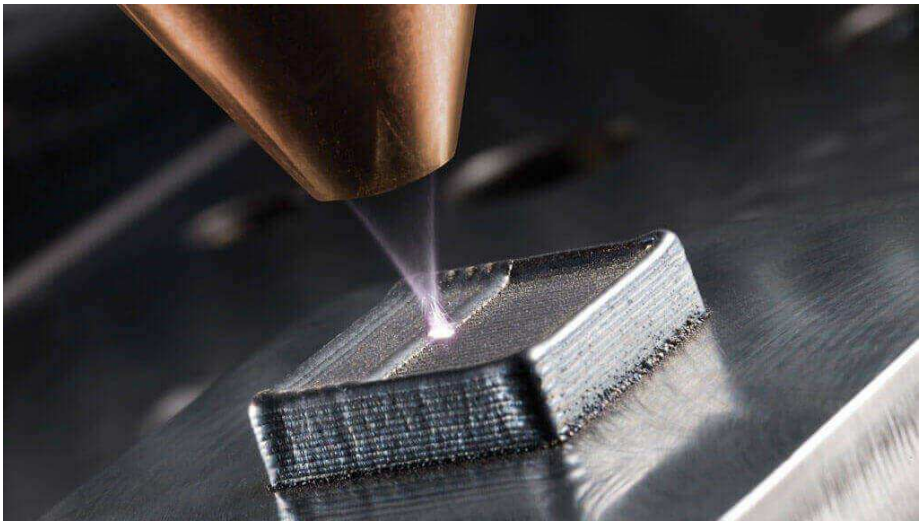

Figure 7: Direct energy deposition technology, electron beam. Image downloaded from https://all3dp.com/1/3d-printing-industry-report-week-33-2018/

1.2.6. Powder Bed Fusion (PBF)

This is a relatively new technology in AM but a promising one especially for the metals industry. According to Forbes article [2] PBF technologies represents more or less the 47% of the usage in all AM world and from this total 33% corresponds to Selective Laser Sintering (SLS). PBF is currently expanding the use of metals as it is observed in the same study, which shows an increment of 5% in the use of Direct Metal Laser Sintering (DMLS) between 2016 and 2017. Taking into account that metals are in the 3rd position of used materials, AM technologies in metals represents more or less the 14% of the total usage. This means that they represent a big share of the industry and it is increasing.

With PBF is possible to create a solid part using a heat source that melts small particles of material powder one layer at a time. The heat source follows the path defined by the cross section of the layer. The part is completed when all layers are added. During buildup of plastics material, the part is surrounded by the powder, acting as supporting material, avoiding deformations during cool down. Unfortunately this doesn't apply for metals. The variety in PBF technologies depend on the different energy sources (for example lasers or electron beams) and the material powder used in the process.

Despite the most common material used are metals and plastics, it is possible to use also ceramics. One main characteristic of PBF parts is the high strength and stiffness that can be achieved, being comparable (or sometimes even better) than the raw material. This is why it is a technology adopted by the industry like for example aeronautics and aerospace, where highly complex and resistant parts are required. Figure 8 shows an example of turbine blades using one of the PBF technologies. It can be seen the high precision and the good surface finish. Another application can be found in the medical field, specifically in prosthetics manufacture since titanium is one of the widely used materials. With PBF is possible to manufacture personalized prosthetics using biocompatible materials, like the hip implant shown in Figure 9.

Figure 8: 3d printed turbine blades on Siemens gas turbines blades. Image downloaded from https://www.siemens.com/innovation/en/home/pictures-of-the-future/industry-and-automation/additive-manufacturing-3d-printed-gas-turbine-blades.html

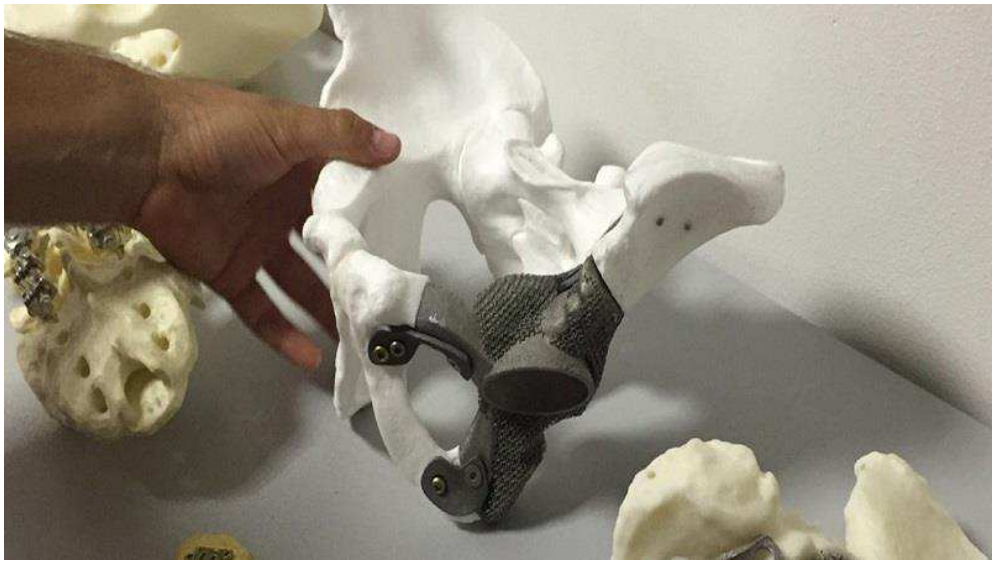

Figure 9: hip implant. Image downloaded from https://www.cellular3d.com/index.php/medical-bioprinting/404-italian-hospital-uses-3d-printed-implants-for-cancer

PBF technologies can be subdivided depending of the used material and technology: basically in polymers and metals. On one hand, Selective Laser Sintering (SLS) is a technology that uses polymers like Nylon, alumide, carbon-fiber filled nylon, PEEK, TPU as base material.

On the other hand, Selective Laser Melting (SLM), Direct Metal Laser Sintering (DMLS) and Electron Beam Melting (EBM) are technologies that uses metals like Aluminum, titanium, stainless steel, nickel alloys, cobalt-chrome as base material. The difference between SLS and SLM is basically the material used and the difference between SLM and DMLS is that SLM achieves full melt of the powder while DMLS heats close to the melting point, sintering the particles. More detailed explanation of SLM technology will be given.

Parts manufactured with PBF are fully functional, which is why this technology is becoming an alternative for conventional manufacturing process. Also, high quality and surface finish can be achieved if compared to DED technologies. However, some of the limitations of PBF technologies are: shrinkage and distortion in the parts, especially in metals where support structures are needed to absorb deformations from residual stresses. Also, closed chamber is required limiting the part size, metal sintering leads to porous and mechanically weak components and in PBF build rates build rates are slow.

Since metals are widely use as functional parts in the industry, due to mechanical, thermal and wear resistance; this work centers the attention in SLM.

SLM

Among all metals additive manufacturing technologies, SLM is the most promising one due to the high accuracy, to its cost, the high surface finish (around 30-60μm), the high strength, the possibility to maintain the original material properties and the availability of materials variety. That is why many companies have been adopting this technology to manufacture metals parts.

Figure 10 shows the sequence of the manufacturing steps of SLM to understand deeply how manufacturing process occur; (1) the leveling blade add powder metal to the current layer, (2) the laser melts the part of the geometry that need to be solidified, (3) build platform moves down making space for the next layer, (4) previous steps are repeated until completing the geometry. When the part is completed, powder is removed to obtain the final piece.

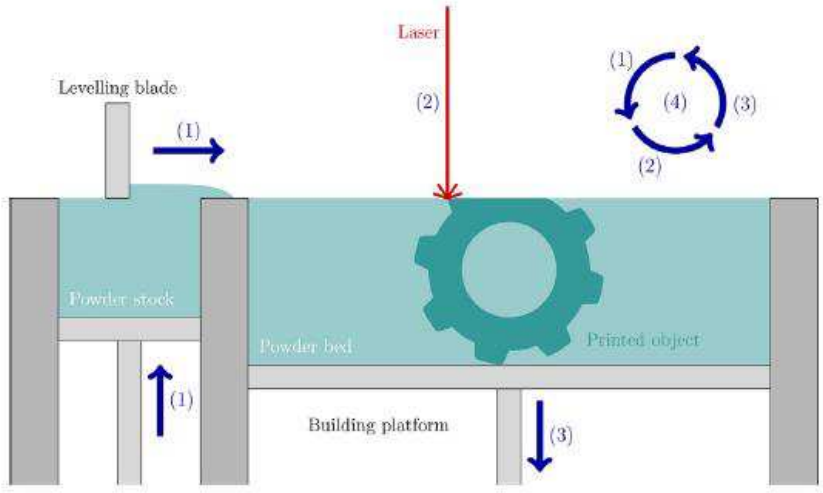

Figure 10: SLM process [3]

SLM is an innovative technology which is expanding and is being progressively adopted by big companies to produce highly complex parts that are not possible to be produced using conventional process like machining, forging or casting. For this reason SLM is a technology that represents a breakthrough in the manufacturing process and it is worth to research in this direction to enhance this technology.

1.3. Current investigations and works objectives

Despite all the advantages that SLM can offer, there are still some unresolved issues with this technology. The concentrated energy input lead to localized high temperature gradients and consequently the formation of residual stresses (RS) and plastics deformation. Normally the finished parts are subjected to heat treatments (like annealing) to reduce residual stresses, but at the same time parts fracture or disconnect from the base plate can occur during build up process. These kinds of problems are difficult to foresee

The amount of RS can sometimes be reduced by modifying scan pattern, the amount of power and scan speed but normally the only way to obtain the optimal parameters is performing expensive trial and error experiments. This increases the costs due to the waste generated, which becomes a point of concern when this technology is used. Other way to optimize the process parameters selection is by predictive methods using computational simulations, which is a more affordable resource that helps to reduce costs in the design process. Computational models are widely used nowadays for this purpose, for example several applications can be found in the foundry industry where design optimization of casted parts is done using mold flow and solidification simulations.

Thermo-mechanical computational models have been used in welding modeling since several years. An example of a thermo-mechanical model developed to simulate a electron beam welding process [4] shows the capabilities that can be achieved using Finite Element Method. Since multi-pass welding processes and AM technologies have a lot of similitudes due to its multi-physics nature, several models can be adapted from Computational Welding Mechanics (CWM) to deal with AM processes simulation. In this sense, there are examples in literature where numerical models are developed for DED technologies like powder blown [5] to successfully simulate all physics involved in an AM process. These kinds of models adopt a fully thermo-mechanical framework and are considered as high fidelity (HF) since the real phenomena involved in the process (like movement of the real welding pool and real path trace followed) is studied.

Normally, HF models make use of mesh size of the same dimension as the deposition. For DED technologies this kind of methods are feasible since the welding deposition is of the order of 1mm for EBAM and 100μm for LENS, in contrast to SLM which handles a deposition of order 10μm. In the literature there are a lot of papers that focuses on the development of high fidelity computational models for SLM that includes all multi-physic phenomena (thermal, mechanical, phase change) and are able to predict the mechanical

behavior of parts [2, 5, 6, 7]. Unfortunately, these models are limited to small parts (around 1.25E-3 cm^3) due to the high computer power needed.

There are studies focused on the understanding of the physical phenomena to try to find the optimal parameters that minimize residual stresses. Experiments to measure RS or distortions are in order to analyze the influence of the process parameters like hatch direction, laser power, scan speed [8,9,10,11]. However some of these researches are limited to small geometries or only to distortions measurements, therefore reliability of the stress results cannot be assured. Note that once the optimized parameters are found for a specific geometry, if it is changed, the experiments must be repeated.

Other investigation line focuses on the micro-scale, studying the evolution of the microstructure during solidification of melted material during SLM [13]. Other investigators also study the influence of plate pre-heating to control the residual stresses [14]. For the sake of simplification, this was not considered in this work, nevertheless it has an undoubtedly influence in the mechanical response of the finished part.

It is seen after some research that numerical models for large geometries are hard to find, due to the mentioned restrains. Since high fidelity models are limited to small geometries, another methods or simplifications are needed to simulate larger and realistic sized problems.

Due to the promising capabilities of SLM technique, the general purpose of this work is the simulation of large geometries fabricated by SLM, tackling the current limitations regarding the complexity of the physical phenomena and the problem size needed.

The two main restrictions that have been identified when trying to simulate large geometries using high fidelity models for SLM, are mentioned as follows. First, the element size required is of order 20μm, due to the actual layer size. To simulate a large component, this element size will result in a problem size that wouldn't be possible to handle. The second restriction is the high computational demand due to the complexity of non-linear transient thermo-mechanical problems.

Therefore, simplified methodologies have to be considered to optimize the modeling at industrial scale level. Two approaches are possible: first, to reduce the computational effort by reducing the model size using a larger mesh size and lumping the layers.

The second approach consists of making engineering assumptions to simplify the physics behind the actual process. In this regard two main simplifications are made to simplify the fully thermo-mechanical problem. The first idea is to solve a mechanical problem predefining the linear shrinkage [15]. That way the original problem is greatly simplified (no phase change considered) and the transient thermal analysis is neglected. Second, adopt the inherent strains method to the SLM simulation. The inherent strains method [16] is a method that has been adapted from the Welding modeling and is a simplification that reduces the plastic problem to a purely elastic analysis, by introducing user defined plastic and thermal strains as equivalent external forces.

Having these simplifications in mind, the objective of this work is to know the accuracy of these methods and assess the error introduced with all assumptions made.

2. Finite Element modeling of SLM

In this section, the computational modeling of this work is explained. First, the weak form and discretization of the heat balance equation is presented, to setup of the high fidelity algorithm. Then, the J2-plasticiy model used to solve the visco-platic behaviour for the stress analysis of the method. Finally, the main assumptions of the inherent strains method are showed.

2.1. Thermal problem

The strong form of the balance of energy governing the thermal problem is:

$$\dot{H} = -\nabla \cdot \mathbf{q} + \dot{Q} + \dot{D}_{mech} \tag{1}$$

Where $\dot{H}$ is the enthalpy rate (per unit of volume), $\mathbf{q}$ is the heat flux, $\dot{Q}$ represents the heat source (per unit of volume) and $\dot{D}_{mech}$ the thermo-mechanical dissipation rate (per unit of volume), respectively. For SLM the heat source is the energy coming from the laser beam and is applied to the molten-pool formed along the scanning path and through the thickness of the deposited material.

The enthalpy is a state variable defined as a function of the temperature T and the liquid fraction:

$$\dot{H} = \rho C\dot{T} + L\dot{f}_L \tag{2}$$

Where ρ is the material density, C is the specific heat, L is the latent heat released during the phase-change process and $\dot{f}_L$ is the change of the liquid fraction parameter. During the phase transformation the material volume, V, can be split into liquid and solid phases as: $V = V_L + V_S$. The liquid and solid fractions are defined as: $f_L = V_L/V$ and $f_S = V_S/V$, respectively, so that: $f_L + f_S = 1$. The evolution of the liquid fraction $\dot{f}_L$ defines how the latent heat is absorbed or released during the phase transformation. The evolution of the liquid/solid fraction is computed based on the multi-nodular theory of nucleation and growth [17].

Remark 1: Considering the case of SLM, the energy coming from the laser beam is extremely high compared to thermo-mechanical dissipation, consequently this terms is neglected.

The heat flux $\mathbf{q}$ is computed according to Fourier's law:

$$\mathbf{q} = -k\nabla T \tag{3}$$

Where k is the thermal conductivity, which is a variable temperature dependent parameter. Then the balance equation for the SLM in his strong form is:

$$\rho C\dot{T} + L\dot{f}_L = \nabla \cdot (k\nabla T) + \dot{Q} \tag{4}$$

To derive the Weak Form of equation (4) let's consider V an open bounded domain in $\mathbb{R}^3$ closed by smooth boundary $S = S_T \cup S_q$, where corresponding Dirichlet (temperatures) boundary conditions are prescribed on S_T and Neumann (flux) boundary conditions on S_q. Suitable initial conditions for the transient problem is defined as $T(t=0) = T_0$. Let's consider a test functions δT defined in the pace of C^1 continuous functions. Then equation (4) is weighted by δT an integrated over V to get:

$$\int_V \left[\rho C\dot{T}\delta T\right] dV + \int_V \left[L\dot{f}_L\delta T\right] dV - \underbrace{\int_V [\nabla \cdot (k\nabla T)\delta T] dV}_{IBP} = \int_V \dot{Q}\delta T dV \tag{5}$$

Integrating by parts (IBP) the 3rd term in the r.h.s:

$$\begin{aligned}\int_V [\nabla \cdot (k\nabla T)\delta T] dV &= -\int_V [k\nabla T \cdot \nabla(\delta T)] dV + \int_V [\nabla \cdot (\delta T k\nabla T)] dV \\ &= -\int_V [k\nabla T \cdot \nabla(\delta T)] dV + \int_S [\delta T(k\nabla T) \cdot \boldsymbol{n}] dS \\ &= -\int_V [k\nabla T \cdot \nabla(\delta T)] dV + \int_S [(\bar{q} + q_{loss})\delta T] dS\end{aligned} \tag{6}$$

Where $\bar{q}$ is the prescribed flux and the parameter q_{loss} is defined as the heat loss by convection, conduction and radiation. The, q_{loss} can be expressed by newton's law [5] as:

$$q_{loss}(T) = HTC_{loss}(T - T_{env}) \tag{7}$$

Where HTC_{loss} is an equivalent heat transfer coefficient that combines conductive, convective and radiation coefficients. When substituting equation ((**6**) in (

(5), the result is the weak form of the energy balance equation:

$$\int_V \left[\rho C \dot{T} \delta T\right] dV + \int_V \left[L \dot{f}_L \delta T\right] dV + \int_V [k \nabla T \cdot \nabla(\delta T)] dV$$
$$= \int_V \dot{Q} \delta T dV + \int_{S_q} q_{loss}(T) \delta T dS + \int_{S_q} \bar{q} \delta T dS \tag{8}$$

Introducing the Backward Euler discretization:

$$\dot{T} = \frac{T^{n+1} - T^n}{\Delta t} \quad \dot{f}_L = \frac{f_L(T^{n+1}) - f_L^n}{\Delta t} \tag{9}$$

Where Δt is the time increment and taking an explicit scheme where all properties are computed in T^n:

$$\int_V \left[\rho C \left(\frac{T^{n+1} - T^n}{\Delta t}\right) \delta T\right] dV + \int_V \left[L \left(\frac{f_L(T^{n+1}) - f_L^n}{\Delta t}\right) \delta T\right] dV + \int_V [k \nabla T \cdot \nabla(\delta T)] dV$$
$$= \int_V \dot{Q} \delta T dV + \int_{S_q} q_{loss}(T) \delta T dS \tag{10}$$

Remark 2: in this work the prescribed flux $\bar{q}$, which correspond to the Neumann boundary condition is considered to be equal to zero.

Then considering a 3D domain discretization using FE, the unknown temperatures and the test functions can be approximated as:

$$T \approx \mathbf{N} \cdot \mathbf{T} \quad \delta T = \mathbf{N} \cdot \boldsymbol{\delta} \mathbf{T}$$

Where **N** is the vector that cotains all shape functions, **T** is the matrix that contains all nodal values of the temperature and **δT** contains nodal values of the test function. When substituting the approximations in the equation ((**10**), the elemental discretized balance equation is:

$$\int_V \left[\rho C \left(\frac{\mathbf{N} \cdot \mathbf{T}^{n+1} - \mathbf{N} \cdot \mathbf{T}^n}{\Delta t}\right) \mathbf{N} \cdot \boldsymbol{\delta} \mathbf{T}\right] dV + \int_V \left[L \left(\frac{f_L(\mathbf{T}^{n+1}) - f_L^n}{\Delta t}\right) \mathbf{N} \cdot \boldsymbol{\delta} \mathbf{T}\right] dV$$
$$+ \int_V [k \nabla \mathbf{N}^T \nabla \mathbf{N}] dV \, \mathbf{T}^{n+1} \boldsymbol{\delta} \mathbf{T} = \int_V \dot{Q} \mathbf{N} \cdot \boldsymbol{\delta} \mathbf{T} dV + \int_{S_q} q_{loss}(T) \mathbf{N} \cdot \boldsymbol{\delta} \mathbf{T} dS \tag{11}$$

$$\left[\int_V \left(\frac{\rho C}{\Delta t}\mathbf{N}^T\mathbf{N}\right)dV\right]\mathbf{T}^{n+1}\boldsymbol{\delta\mathbf{T}} + \left[\int_V (k\nabla\mathbf{N}^T\nabla\mathbf{N})dV\right]\mathbf{T}^{n+1}\boldsymbol{\delta\mathbf{T}} + \int_V \left[\frac{L}{\Delta t}f_L(\mathbf{T}^{n+1})\mathbf{N}\right]dV\boldsymbol{\delta\mathbf{T}}$$
$$= \left[\int_V \left(\frac{\rho C}{\Delta t}\mathbf{N}^T\mathbf{N}\right)dV\right]\mathbf{T}^{n}\boldsymbol{\delta\mathbf{T}} + \int_V \left(\frac{L}{\Delta t}f_L^n\mathbf{N}\right)dV\boldsymbol{\delta\mathbf{T}} + \int_V \dot{Q}\mathbf{N}dV\boldsymbol{\delta\mathbf{T}}$$
$$+ \int_{S_q} q_{loss}(T)\mathbf{N}dS\boldsymbol{\delta\mathbf{T}}$$

After assembling, the final system can be written in matrix form as:

$$\left[\frac{\mathbf{M}}{\Delta t} + \mathbf{K}\right]\mathbf{T}^{n+1} + \frac{\mathbf{l}(\mathbf{T}^{n+1})}{\Delta t} = \frac{\mathbf{M}}{\Delta t}\mathbf{T}^n + \frac{\mathbf{l}^n}{\Delta t} + \mathbf{f} + \mathbf{q}(\mathbf{T}^n) \tag{12}$$

Where **T** is the vector of the nodal elemental contributions of the temperature; **M** and **K** are the global assembled mass and conduction matrixes, and **l**, **f**, **q** is the latent heat vector, heat source vector and heat flux vector, respectively.

2.2. Mechanical problem

To solve the mechanical problem, the quasi-static balance of momentum equation must be solved. The local form of the governing equation consists in find the displacement field **u** for a given prescribed body forces **b** so that:

$$\nabla\cdot\boldsymbol{\sigma}(\mathbf{u}) + \mathbf{b} = \mathbf{0} \tag{13}$$

Where $\boldsymbol{\sigma}$ is the Cauchy's stress tensor. In order to address the visco-plastic mechanical behavior, the stress tensor is split into hydrostatic and deviatoric parts as:

$$\boldsymbol{\sigma}(\mathbf{u},p) = \frac{1}{3}\mathrm{tr}(\boldsymbol{\sigma})\mathbf{I} + dev(\boldsymbol{\sigma}) = p\mathbf{I} + \mathbf{s}(\mathbf{u}) \tag{14}$$

Where p is the hydrostatic pressure and **s** is the deviatoric stress tensor. This form is convenient to deal with the isochoric behavior, when the deformations are mainly deviatoric. This is the case of J2-pasticity models which are commonly used to describe the constitutive behavior of metallic alloys. Then, substituting equation ((**14**) in (13), the local form of the balance momentum equation is rewritten as:

$$\nabla\cdot\mathbf{s}(\mathbf{u}) + \nabla p + \mathbf{b} = \mathbf{0} \tag{15}$$

Recalling the definition the strain tensor and its volumetric and deviatoric parts:

$$\begin{aligned} \boldsymbol{\varepsilon} &= \nabla^s \mathbf{u} \\ e^{vol} &= tr(\boldsymbol{\varepsilon}) = \nabla \cdot \mathbf{u} \\ \mathbf{e} &= dev(\boldsymbol{\varepsilon}) = \boldsymbol{\varepsilon} - \frac{tr(\boldsymbol{\varepsilon})}{3}\mathbf{I} \end{aligned} \tag{16}$$

Where $\boldsymbol{\varepsilon}$ is the total strains tensor, e^{vol} is the volumetric part of the total strain tensor and $\mathbf{u}$ the displacement field. Recalling the additive split property of strains it is possible to express the total strains in terms of elastic, visco-plastic and thermal strains as:

$$\boldsymbol{\varepsilon} = \boldsymbol{\varepsilon}^e + \boldsymbol{\varepsilon}^{vp} + \boldsymbol{\varepsilon}^{th} \tag{17}$$

Where $\boldsymbol{\varepsilon}^e$ is the elastic strain tensor, $\boldsymbol{\varepsilon}^{vp}$ is the visco-plastic strain tensor and $\boldsymbol{\varepsilon}^{th}$ is the thermal strains tensor. Then, considering that $\boldsymbol{\varepsilon}^{vp}$ is purely deviatoric and $\boldsymbol{\varepsilon}^{th}$ is purely volumetric, the split constitutive equations are:

$$\begin{aligned} p &= \frac{K}{f_S}(e^{vol} - e^T) \\ \mathbf{s} &= \frac{2G}{f_S}(\mathbf{e} - \mathbf{e}^{vp}) \end{aligned} \tag{18}$$

Where e^T is the thermal deformation, K is the temperature dependent bulk modulus and G is the temperature dependent shear modulus. With this formulation is possible to deal with compressible and incompressible cases (liquid and solid phases) in a simple way. The final problem consists of finding the displacement field $\mathbf{u}$ and pressure p such as the following equations hold:

$$\begin{aligned} \nabla \cdot \mathbf{s}(\mathbf{u}) + \nabla p + \mathbf{b} &= \mathbf{0} \\ p = \frac{K}{f_S}(e^{vol}(\mathbf{u}) - e^T(T)) \end{aligned} \tag{19}$$

The thermal deformation $\boldsymbol{\varepsilon}^{th}$ is defined as a volumetric term of the form:

$$\begin{aligned} \boldsymbol{\varepsilon}^{th} &= e^T(T)\mathbf{I} \\ e^T(T) &= \begin{cases} e^{ph}(T) & if\ T_S \le T \le T_L \\ e^{cool}(T) & otherwise \end{cases} \end{aligned} \tag{20}$$

Where e^{cool} is the thermal deformation, e^{ph} is the shrinkage due to the phase transformation; T_S and T_L are the solidus and liquidus temperature, respectively. The thermal shrinkage is due to the density variation in the solidification interval $T_S \le T \le T_L$ and is expressed as:

$$\frac{de^{ph}}{dt} = -\frac{1}{\rho}\frac{d\rho}{dt} \tag{21}$$

After integrating equation (21):

$$e^{ph} = ln\frac{\rho(T_0)}{\rho(T)} \cong \frac{\rho_0 - \rho(T)}{\rho_0} \tag{22}$$

Where ρ_0 is the value of the density at the initial temperature T_0 and it is defined as:

$$\rho_0 = \begin{cases} \rho_S = \rho(T_S) & if\ T_0 \leq T_S \\ \rho_L = \rho(T_L) & if\ T_0 \geq T_L \end{cases} \tag{23}$$

Then, the thermal deformation e^{cool} is computed as:

$$e^{cool}(T) = 3[\alpha(T)(T - T_{env}) - \alpha(T_0)(T_0 - T_{env})] \tag{24}$$

Where $\alpha(T)$ is the temperature dependent secant thermal expansion coefficient and T_{env} is the room temperature.

To derive the Weak Form of equations (19), let's consider V an open bounded domain in $\mathbb{R}^3$ closed by smooth boundary $S = S_u \cup S_\sigma$ where corresponding Dirichlet (displacements) boundary conditions are prescribed on S_u and Neumann (tractions) boundary conditions on S_σ. Suitable initial conditions for the transient problem is defined as $\mathbf{u}(t=0) = \mathbf{u}_0$ and $\bar{\mathbf{t}}(t=0) = \bar{\mathbf{t}}_0$. Let's consider a set of test functions $\delta\mathbf{u}$ and δp defined in the pace of C^1 continuous functions. Then, equations (19) are multiplied by $\delta\mathbf{u}$ and δp and integrated over V to derive the weak form:

$$\underbrace{\int_V \left[\left(\nabla \cdot \mathbf{s}(\mathbf{u})\right)\delta\mathbf{u}\right]dV + \int_V (\nabla p \cdot \delta\mathbf{u})dV}_{IBP} + \int_V (\mathbf{b} \cdot \delta\mathbf{u})dV = \mathbf{0}$$
$$\int_V \left[\left(\nabla \cdot \mathbf{u} - e^T - \frac{p}{K}\right)\delta p\right]dV = 0 \tag{25}$$

Integrating by parts the terms indicated in the r.h.s. of equation (25):

$$\int_V \left[\left(\nabla \cdot \mathbf{s}(\mathbf{u})\right)\delta\mathbf{u}\right]dV + \int_V (\nabla p \cdot \delta\mathbf{u})dV$$
$$= -\int_V (\mathbf{s}(\mathbf{u}) : \nabla^s \delta\mathbf{u})dV - \int_V (p\nabla \cdot \delta\mathbf{u})dV + \int_{S_\sigma} (\bar{\mathbf{t}} \cdot \delta\mathbf{u})dS \tag{26}$$

Where $\bar{\mathbf{t}}$ are the prescribed tractions. Then, when substituting equation (26) in (25) the weak form of the mechanical quasi-static problem is:

$$\int_V (\mathbf{s}(\mathbf{u}):\nabla^s \delta\mathbf{u})dV + \int_V (p\nabla\cdot\delta\mathbf{u})dV = \int_V (\mathbf{b}\cdot\delta\mathbf{u})dV + \int_{S_\sigma} (\bar{\mathbf{t}}\cdot\delta\mathbf{u})dS \quad \forall\delta\mathbf{u}$$
$$\int_V [(\nabla\cdot\mathbf{u})\delta p]dV - \int_V \left[\frac{p}{K}\delta p\right]dV = \int_V [e^T\delta p]dV \quad \forall\delta p \tag{27}$$

In order to solve the plastic model and obtain the value of the visco-plastics strains $\mathbf{e}^{vp}$, the following variable must be defined. First the J2-yield surface:

$$\Phi(\mathbf{s}, q_h, T) = \|\mathbf{s}\| - f_s R(q_h, T) \tag{28}$$

Where R is the yield surface radius and q_h is the stress like isotropic hardening and are defined as:

$$R(q_h, T) = \sqrt{\frac{2}{3}}\left[\sigma_y(T) - q_h\right] \tag{29}$$

$$q_h(\xi, T) = \left[\sigma_\infty(T) - \sigma_y(T)\right][1 - \exp(-\delta(T)\xi)] - h(T)\xi \tag{30}$$

Where σ_y is the initial yield stress (elastics limit), $h(T)$ and $\delta(T)$ are the coefficients which control the linear and the exponential isotropic hardening laws, respectively; $\sigma_\infty(T)$ is the saturation flow stress parameter and ξ is the isotropic strain variable and which expression is:

$$\dot{\xi} = \dot{\gamma}^{vp}\frac{\partial\Phi(\mathbf{s}, q_h, T)}{\partial q_h} = \dot{\gamma}^{vp}\sqrt{\frac{2}{3}}f_s \tag{31}$$

Then, visco-plastic strain evolution is defined as:

$$\dot{\mathbf{e}}^{vp} = \dot{\gamma}^{vp}\frac{\partial\Phi(\mathbf{s}, q_h, T)}{\partial\mathbf{s}} = \gamma^{vp}\frac{\mathbf{s}}{\|\mathbf{s}\|} \tag{32}$$

And the visco-plastic multiplier:

$$\dot{\gamma}^{vp} = \left\langle\frac{\Phi(\mathbf{s}, q_h, T)}{\eta}\right\rangle^{1/m} \tag{33}$$

In this model, when material is completely liquid ($T > T_L$) the solid fraction is equal to zero. Taking to account this, equation (18) changes to:

$$f_S p = K(e^{vol} - e^T) = 0 \rightarrow e^{vol} - e^T = 0 \rightarrow \nabla\cdot\mathbf{u} - e^T = 0$$
$$f_S\mathbf{s} = 2G(\mathbf{e} - \mathbf{e}^{vp}) = \mathbf{0} \rightarrow \mathbf{e} - \mathbf{e}^{vp} = \mathbf{0} \tag{34}$$

If both equations are combined, it is seen that the volumetric and the deviatoric components of the elastic strain tensor are zero. Also, it is seen that first equation corresponds to the continuity equation of mass conservation and the second implies that only shear deformations are present.

The yield-surface radius defined in equation (29) reduces as the temperature increases until vanishing (*R=0*) above the liquidus temperature. Taking this into account in the evolution law of the plastic multiplier (33), a purely viscous model is recovered:

$$\mathbf{s} = \eta(\gamma^{vp})^{m-1}\dot{\mathbf{e}}^{vp} \tag{35}$$

The shape functions used for the discretization are:

$$\mathbf{u} \approx \mathbf{N}\cdot\mathbf{U} \quad \boldsymbol{\delta}\mathbf{u} = \mathbf{N}\cdot\boldsymbol{\delta}\mathbf{U} \quad p \approx \mathbf{N}\cdot\mathbf{P} \quad \delta p \approx \mathbf{N}\cdot\boldsymbol{\delta}\mathbf{P}$$

Where **U** is the vector of nodal values of the displacements, **P** is the vector nodal values of pressure and **N** is the vector of all shape functions.

The discretized Weak Form is:

$$\begin{gathered}\int_V \left(\mathbf{s}^{\boldsymbol{h}}\nabla^s\mathbf{N}\right)dV\boldsymbol{\delta}\mathbf{U} + \left\{\int_V [\mathbf{N}(\nabla\cdot\mathbf{N})]dV\right\}\mathbf{P}\boldsymbol{\delta}\mathbf{U} = \int_V (\mathbf{b}\cdot\mathbf{N})dV\boldsymbol{\delta}\mathbf{U} + \int_{S_\sigma}(\bar{\mathbf{t}}\cdot\mathbf{N})dS\boldsymbol{\delta}\mathbf{U} \\ \left\{\int_V [(\nabla\cdot\mathbf{N})\mathbf{N}]dV\right\}\mathbf{U}\boldsymbol{\delta}\mathbf{P} - \left\{\int_V \frac{1}{K}[\mathbf{N}^T\mathbf{N}]dV\right\}\mathbf{P}\boldsymbol{\delta}\mathbf{P} = \int_V [e^T\mathbf{N}]dV\boldsymbol{\delta}\mathbf{P}\end{gathered} \tag{36}$$

Where $\mathbf{s}^h$ is the discrete deviatoric stress tensor. It can be noticed that the mechanical problem presented is non-linear and must be solved using an iterative method. In this sense Newton-Raphson has shown to be a very efficient and reliable method to solve non-linear system of equations.

To derive the NR method, a first order Taylor expansion is approximated to the value of the function, taking into account that system of equations (27) can be written in short form as **F**(**u**,*p*)=**0**:

$$\mathbf{0} = \mathbf{F}(\mathbf{u}^{k+1}, p^{k+1}) \approx \mathbf{F}(\mathbf{u}^k, p^k) + \frac{\partial\mathbf{F}(\mathbf{u}^k, p^k)}{\partial(\mathbf{u}, p)}\Delta(\mathbf{u}, p)^{k+1} \tag{37}$$

Where the Jacobian matrix $\frac{\partial\mathbf{F}(\mathbf{u}^k,p^k)}{\partial(\mathbf{u},p)}$ is computed as follows:

$$\frac{\partial\boldsymbol{F}}{\partial(\mathbf{u},p)} = \begin{bmatrix}\dfrac{\partial\boldsymbol{F}_1}{\partial\mathbf{u}} & \dfrac{\partial\boldsymbol{F}_1}{\partial p} \\ \dfrac{\partial\boldsymbol{F}_2}{\partial\mathbf{u}} & \dfrac{\partial\boldsymbol{F}_2}{\partial p}\end{bmatrix}$$

Then, the Newton-Raphson scheme is the following:

i. Make an initial guess $\{\mathbf{u}^k, p^k\}$
ii. Solve $\frac{\partial \mathbf{F}(\mathbf{u}^k, p^k)}{\partial(\mathbf{u}, p)} \Delta(\mathbf{u}, p)^{k+1} = -\mathbf{F}(\mathbf{u}^k, p^k)$
iii. $(\mathbf{u}^{k+1}, p^{k+1}) = (\mathbf{u}^k, p^k) + \Delta(\mathbf{u}, p)^{k+1}$
iv. Repeat until convergence is achieved

2.3. Born-dead-element technique

The layer-by-layer attribute of the AM processes requires a special treatment to determine the actual volume on which the problem should be solved. An algorithm is needed to identify the elements at which the laser energy should be applied and add them to the problem domain. The born-dead-element technique [3] is a search algorithm that is able to classify the elements in active, inactive and activated elements.

To explain this technique, let's consider the manufacturing of a cubic geometry and let's assume that it is sliced in 100 layers. Let's consider that the layer number 20 is currently being deposited. The *active* elements in this example are the ones activated in previous steps, which are within layer 1-19. These elements are computed and assembled into the global matrix. The *inactive* elements in this example are the ones within layers 21-100 (not yet built) and the elements that have not been activated on layer 20, because laser beam has not passed through them. These elements are not included as part of the computational domain in the current mechanical step. The *activated elements* are the ones that change from inactive to active in one time-step.

The advantage of this technique is that it brings the possibility of defining a computational mesh independently of the scanning path. In other words, after the geometry is meshed, the buildup process is simulated by activating elements following the scanning sequence. Since the element activation resembles the movement of the heat source, it is a technique widely used in PBF technologies.

2.4. The Inherent Strain Method for SLM

The origin of the Inherent Strain Method is directly related to Computational Welding Mechanics and it has been widely used [18], because it allows the simplification of a non-linear transient thermo-mechanical problem to a simpler quasi-static mechanical problem. The main characteristic is that the values of thermal and/or plastic strains (or inherent strains) are defined by the end-user. If thermal and plastic strains are predefined, the split of the balance of momentum equation is no longer needed. Therefor the equation (13) is the one solved, which leads to a linear elastic system of equations as it will be shown. When strain tensor definition (eq. (16)) is substituted in the constitutive equations (18), is it possible to express the divergence of Cauchy's stress as follows:

$$\nabla \cdot \boldsymbol{\sigma} = (K + G)\nabla(\nabla \cdot \mathbf{u}) + \mathrm{G}\nabla \cdot \nabla \mathbf{u} \tag{38}$$

Since there's no variation of density and any other property in time, the mass balance equation results in $\nabla \cdot \mathbf{u} = 0$. Consequently, equation (38) is simplified and after substituting in the balance momentum equation, the weak form can be obtained:

$$\underbrace{\int_V [(\mathrm{G}\nabla \cdot \nabla \mathbf{u}) \cdot \delta \mathbf{u}] dV}_{IBP} + \int_V (\mathbf{b} \cdot \delta \mathbf{u}) dV = 0$$

$$\int_V [\mathrm{G}\nabla \mathbf{u} : \nabla \delta \mathbf{u}] dV - \int_{S_\sigma} (\bar{\mathbf{t}} \cdot \delta \mathbf{u}) dS + \int_V (\mathbf{b} \cdot \delta \mathbf{u}) dV = \mathbf{0} \tag{39}$$

After the discretization, the assembled system of equations is:

$$\left\{ \int_V [\mathrm{G}\nabla \mathbf{N}^T \nabla \mathbf{N}] dV \right\} \mathbf{U} \cancel{\delta \mathbf{U}} = \int_{S_\sigma} (\bar{\mathbf{t}} \cdot \mathbf{N}) dS \cancel{\delta \mathbf{U}} - \int_V (\mathbf{b} \cdot \mathbf{N}) dV \cancel{\delta \mathbf{U}}$$

$$\mathbf{K}\mathbf{U} = \mathbf{f} \tag{40}$$

Where **K** is the stiffness matrix and **f** is the force vector that includes contribution of body forces and superficial tensions. Then, strain and stress tensors are recovered considering the equations (16) and (17):

$$\boldsymbol{\varepsilon} = \nabla \mathbf{N} \mathbf{U}$$

$$\boldsymbol{\sigma} = \mathbf{D}^e \boldsymbol{\varepsilon}^e = \mathbf{D}^e (\boldsymbol{\varepsilon} - \boldsymbol{\varepsilon}^{vp} - \boldsymbol{\varepsilon}^{th}) \tag{41}$$

Where $\mathbf{D}^e$ is the elastic constitutive tensor. In this work two main methods are developed: in one only thermal strains are predefined and in the second thermal and plastic strains are predefined.

In the first method, the value of $\boldsymbol{\varepsilon}^{th}$ (thermal deformation) is defined as an input for the model. The value is prescribed by specifying the temperature T in equation (24) and material is considered to be always solid (f_S=1) after each step. With this simplification, the temperature problem is no longer needed for the mechanical problem. Therefore, time dependency and thermal influence are neglected after this assumption. In this work, this model is named "shrinkage" and it requires the solution of equation (36) which requires the use of the J2-plasticity model. In summary, $\boldsymbol{\varepsilon}^{th}$ is computed using the predefined value of T^{inh} as follows:

$$\boldsymbol{\varepsilon}^{th} = 3\left[\alpha\left(T^{inh}\right)\left(T^{inh} - T_{env}\right) - \alpha(T_0)(T_0 - T_{env})\right]\mathbf{I} \tag{42}$$

In the second method, both thermal deformation $\boldsymbol{\varepsilon}^{\mathrm{th}}$ and visco-plastic deformation $\boldsymbol{\varepsilon}^{\mathrm{vp}}$ are defined by the end-user. That way neither temperature values nor the solution of J2-plasticity model is needed. In this case, the equation (40) is solved and the values of the strains and the stresses are recovered using equation (41). In summary, $\boldsymbol{\varepsilon}^{th}$ is obtained using the equation (42) and $\boldsymbol{\varepsilon}^{\mathrm{vp}}$ is obtained using a predefined scalar parameter called e^{inh} as follows:

$$\boldsymbol{\varepsilon}^{vp} = e^{inh}\begin{bmatrix}1 & 0 & 0\\ 0 & 1 & 0\\ 0 & 0 & -2\end{bmatrix} \tag{43}$$

With these simplifications it is possible to reduce significantly the computation time required to solve the SLM simulation, as other researches have demonstrated by adapting the Inherent Strain Method to Powder Bed Fusion (PBF) processes in a multi-scale simulation framework [19].

It can be seen that using Inherent Strains Method, there is no time discretization needed since the problem is discretized in mechanical steps, which depends on the scanning path, the number of hatches and the number of layers defined. Considering the hypothesis previously mentioned, the next step is to check that is possible to recover the actual mechanical behavior using the inherent strains method.

3. Measure technologies

One crucial point in every research is the validation of the computational models, being the residual stresses one of the major concerns. In this section, the intention is to present the technologies available to measure residual strains/stresses in parts build with SLM. For example, photo-stress coating is a qualitative technique that consists on applying a special coating that reacts with the material, showing different colors depending of the load applied. This technique helps to identify zones with high stress, but it is limited to superficial results and large parts.

If quantitative results are needed, the most common methods involve strain gages measurement and diffraction techniques. In this sense, X-ray diffraction, hole drilling and neutron diffraction techniques are explained in the following section, since they are the commonly used for metals.

3.1. X-ray diffraction

This method offers a high accuracy but it is limited to superficial measurements (8-20μm), which makes it suitable for very thin parts. The X-ray diffraction is not only used to measure strains but also to determine unit cell dimension, to measure purity, to characterize crystalline material and others. The main parameter that is possible to obtain with this technique is the inter-planar distance of the lattice planes, parameter “d” in Figure 11. This distance can be compared to the value of an unloaded unit cell and the difference will give the amount of deformation.

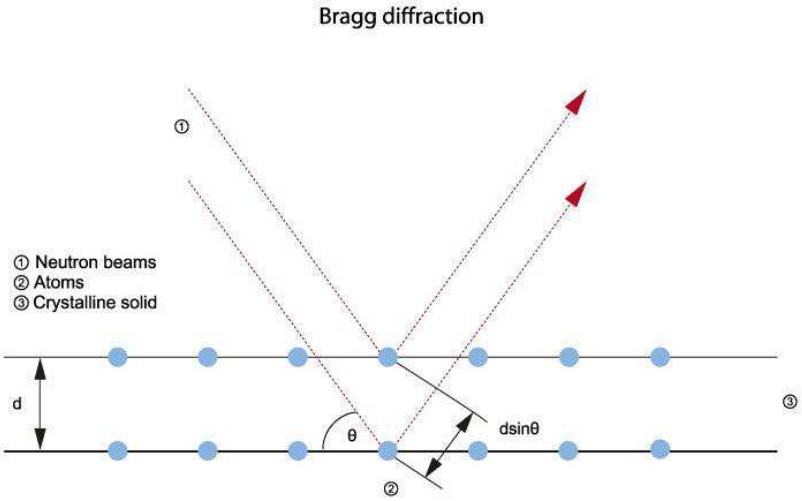

Figure 11: scheme of how diffraction works

Let's explain roughly how this technology works. The X-rays are generated at different wavelengths "λ" and directed at different incident angle "2θ" towards the sample. The X-rays are scattered in a specular fashion by the atoms in the material and the diffracted ones are detected and counted. Using Bragg's Law ($n\,\lambda = 2d.\sin(\theta)$) is possible to relate the wavelength of the electromagnetic radiation to the diffraction angle and the lattice spacing in a crystalline sample.

After scanning, all possible diffraction directions of the lattice are obtained due to the random orientation of the solidified material. Conversion of the diffraction peaks to d-spacings allows the computation of residual strains when comparing to the d-spacings of the unloaded lattice. Then residual stresses can be computed using corresponding constitutive equations.

The main drawbacks of this method are: the limitation of superficial measurements and its cost, which can be 4-10 times comparing to the hole drilling method.

3.2. Hole drilling

This method is one of the most popular and ancient. It is quicker to perform, due to the easy set-up. Is a recommended method to detect cracks bellow surface, or distortions on thin parts. With this method it is possible to measure residual stress at a surface depth of 2mm.

To make the measurement, a strain-gage rosette is glued to the sample in the area of interest. The rosette typically consists of three strain gages arranged at 0 degrees, 90 degrees, and 135 degrees around a center point where the hole is drilled (see Figure 12). Once the hole is drilled, the residual stresses are released and the change of strains is measured. Then, the deformations obtained are converted to stresses using constitutive equations.

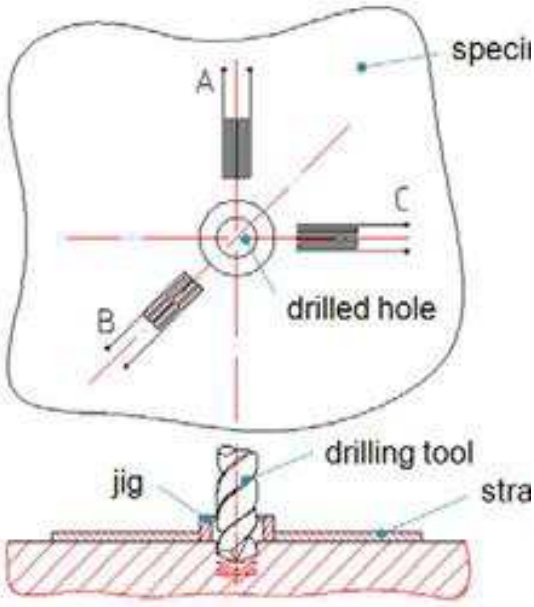

Figure 12: gage arrangement for hole drilling

The rosettes are commercially available from different hole diameters (1,6 – 6,3mm), but small size are preferred to reduce stresses induced by the drilling. One of the biggest constrain in this method is the milling speed, which is required to be of the order of 10^5 rpm to drill without introducing new stresses to the specimen. The problem is that normally the available equipment drills at a speed of order 10^3 rpm introducing measurement errors.

The maximum depth of measurement is limited by the diameter of the hole drilled by the ultra-high speed mill. The data that is possible to retrieve is the biaxial stresses and shear stresses. However, Hole Drilling is limited to measurement at the surface level (max 2mm). To be able to measure interior surface, additional cuts are needed, but the cuts will relax the part changing the initial stress configuration.

3.3. Neutron diffraction

This method is considered to be the best stress measurement technique due to its highly accuracy and capacity of measure inner surfaces. Unfortunately, this technique is not widely available and it is expensive since it requires a nuclear reactor to supply the neutrons beam. Other limitations are regarding the samples size; however mechanical parts of size of order x10mm can be measured. This technique allows the collection of a full stress tensor, or simple tri-axial stresses, depending on how many vectors are measured.

The functional principle of this method is exactly the same as the one of the X-ray diffraction technique. The difference is that instead of using an electromagnetic wave, a neutron beam is used, being able to penetrate the object more deeply. Beam penetration is about 152 mm in aluminum and about 38 mm in iron and steel and sampling volumes can vary from 0.15 mm to 20 mm on a side, depending on the grain size of the material.

Neutron diffraction is a very powerful technique, due to its non-destructive nature and since data can be acquired from large parts or assemblies, either of which can subsequently be placed in service and then re-evaluated. It removes the necessity for cutting up many specimens, considering the inaccuracies that the cuts may lead to.

Some drawbacks may include the time collection for data and the inability to acquire surface data. Furthermore, the technique can be tremendously expensive for many corporate research budgets. The other major difficulty is the limited number of facilities available in the world that counts with this kind of machines.

Fortunately, the National Institute of Standards and Technology (NIST) have performed measurement of residual strains in parts built using SLM and the results are available for the public. This data is crucial for this work to be able to validate the proposed models.

4. Experimental set-up

The experimental data is taken from a benchmark study performed by the National Institute of Standards and Technology [20] from which two kinds of results are obtained. The first experimental data is the distortion after cutting part of the sample. The second is the measure of the residual strains field using neutron diffraction technology.

First, the geometry of the built sample is shown in Figure 13. It consist of a Cantilever of 75mm long, 12mm tall, and 5mm wide with 7mm tall 'legs' that form into 45° overhangs below a solid structure and have different thicknesses. This kind of geometry is one of the most common in AM experiments, since it allows the measurement of the distortion, which is a very easy and quick way to validate results.

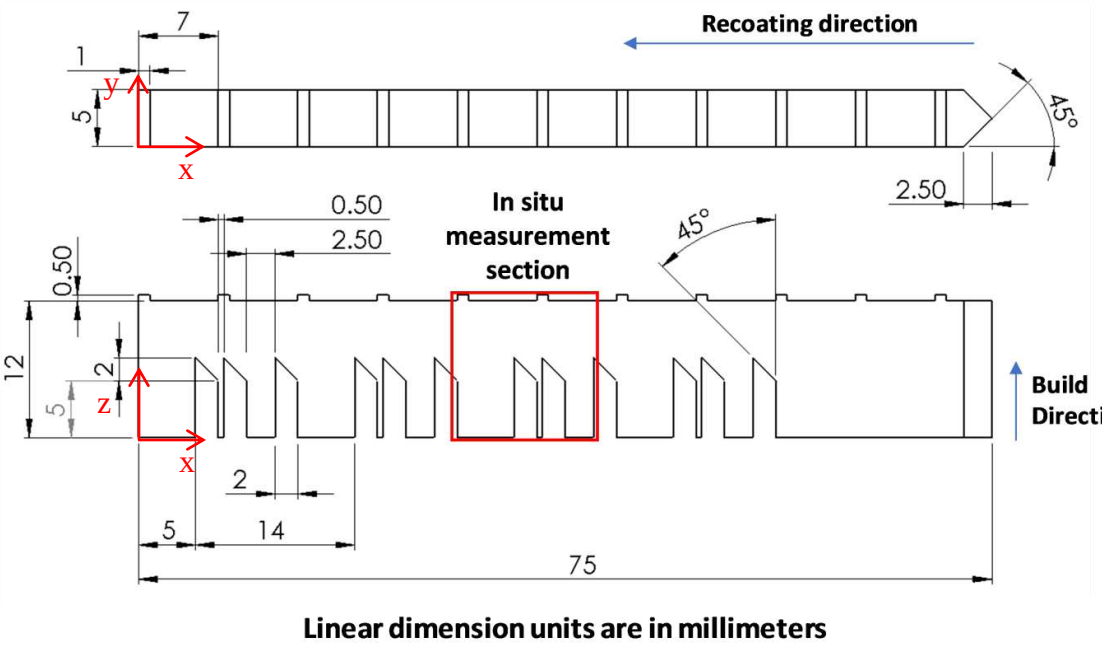

Figure 13: cantilever geometry used for models validation [20]

The material used to build this geometry is the nickel-based super-alloy IN625 with material properties of Table 1 and the chemical composition showed in the original study [20].

Table 1: Elastic Properties of Inconel 625

Property	Value	Unit
Density	8440	kg/m^3
Thermal dilatancy	13e-6	µm/µm-°C
Young Modulus	207	GPa
Poisson Ratio	0.278	-

The PBF machine used is a *EOS M270* also called CBM in the benchmark, which stands for commercial build machine and a summary of the build parameters are shown in Table 2:

Table 2: built parameters of the Cantilever

Parameter and description	CBM Machine
Total number of layers	625
Layer height	20 µm
Contour Scan speed	900 mm/s
Contour Laser power	100 W
Infill Scan Speed	800 mm/s
Infill Laser Power	195 W
Hatch Distance	100 µm
Inert gas	Nitrogen
Oxygen level	≈ 0.5%

Extended information about the scanning sequence and other experiments conducted can be found in the mentioned benchmark study.

4.1. Results of part distortion

After the buildup process, the object is subjected to residual stresses that are not able to release since the part is attached to the substrate. One way to quantify the amount of elastic energy accumulated in the sample, is to cut part of it and measure the distortion after stress release. The step by step procedure is explained following.

Before starting the measure, the tops of the 11 ridges are ground to remove the surface roughness to be able to accurately measure with a coordinate measuring machine (CMM). To obtain the object's distortion, the first step is to measure the initial vertical position of each ridge. Then, the legs are cut using wire electron discharges machining (EDM) following the red line in Figure 14. Consequently, the part deflects upward (yellow line in Figure 14) due to relaxation of the as-built residual stresses and new vertical position is measured. The displacements are obtained by computing the variation of ridges position and the results for the IN625 are shown in Figure 14.

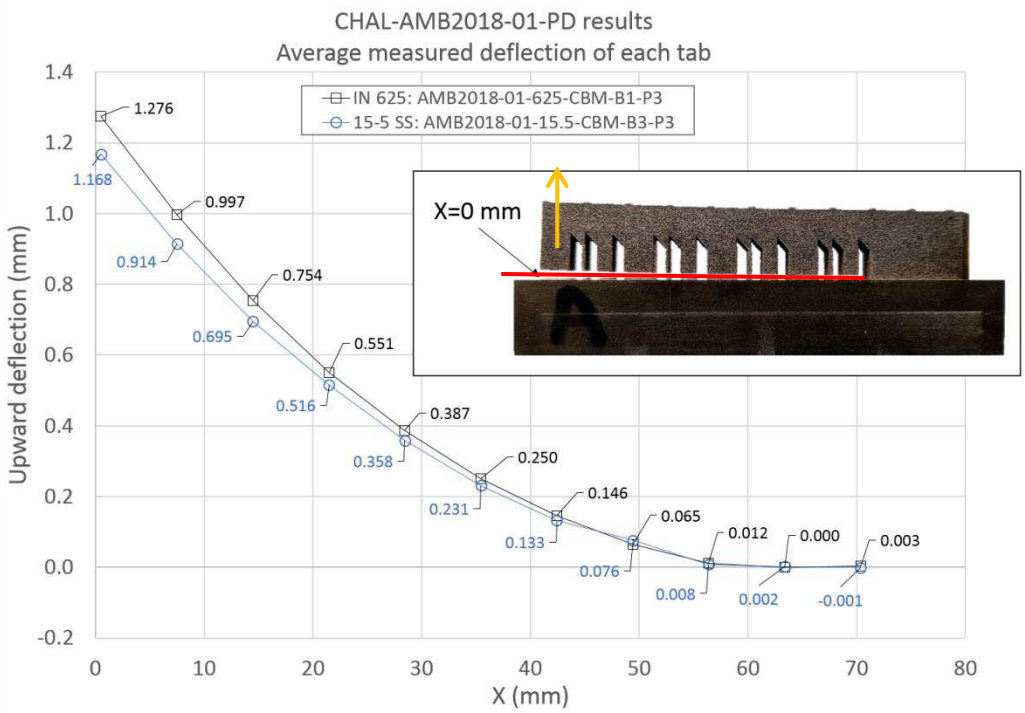

Figure 14: results of the distortion in z [20]

It is seen that the deformation of the Cantilever is more or less quadratic. This deformation is one of the key points regarding the need of support structures in SLM. Inappropriate selection of support structure will lead to deformations like this one during build up, risking the machine's operation. For a part that is more or less 70mm long, a deflection of 1.3mm is considered high comparing to other manufacturing process.

4.2. Results of residual strains/stress

Prior to the EDM cut, the Residual elastic strain (RS) within the as-built IN625 part is measured using a BT8 diffractometer at the NIST Center for Neutron Research (NCNR), which uses neutron diffraction technology. Figure 15 indicates the measurement positions for lattice strains on the X-Z plane centered on the midline of the specimen. Strains along the *xx*, *yy*, *zz* directions are measured considering that measurement gauge volume is approximately a cube with edges that measure 1.5 mm. From this data, the values of stresses are estimated using the value of elastic modulus, Poisson ratio and the constitutive equations. The results in each direction are shown in Figure 16.

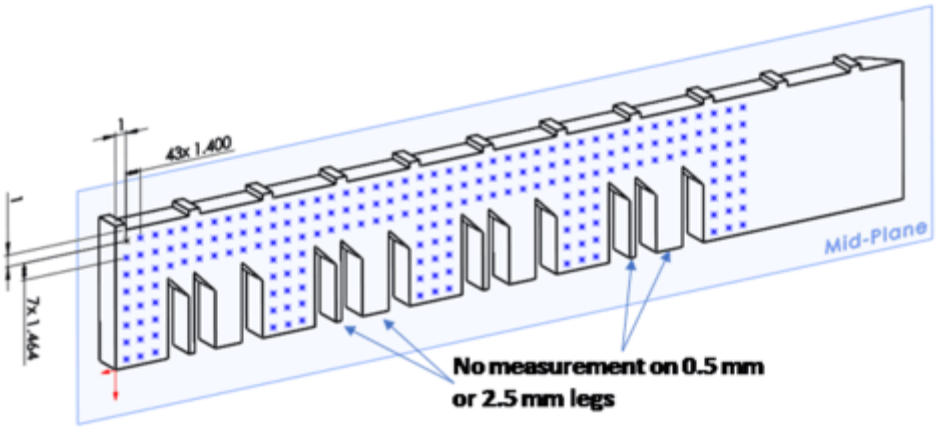

Figure 15: measurement points of the residual stresses [20]

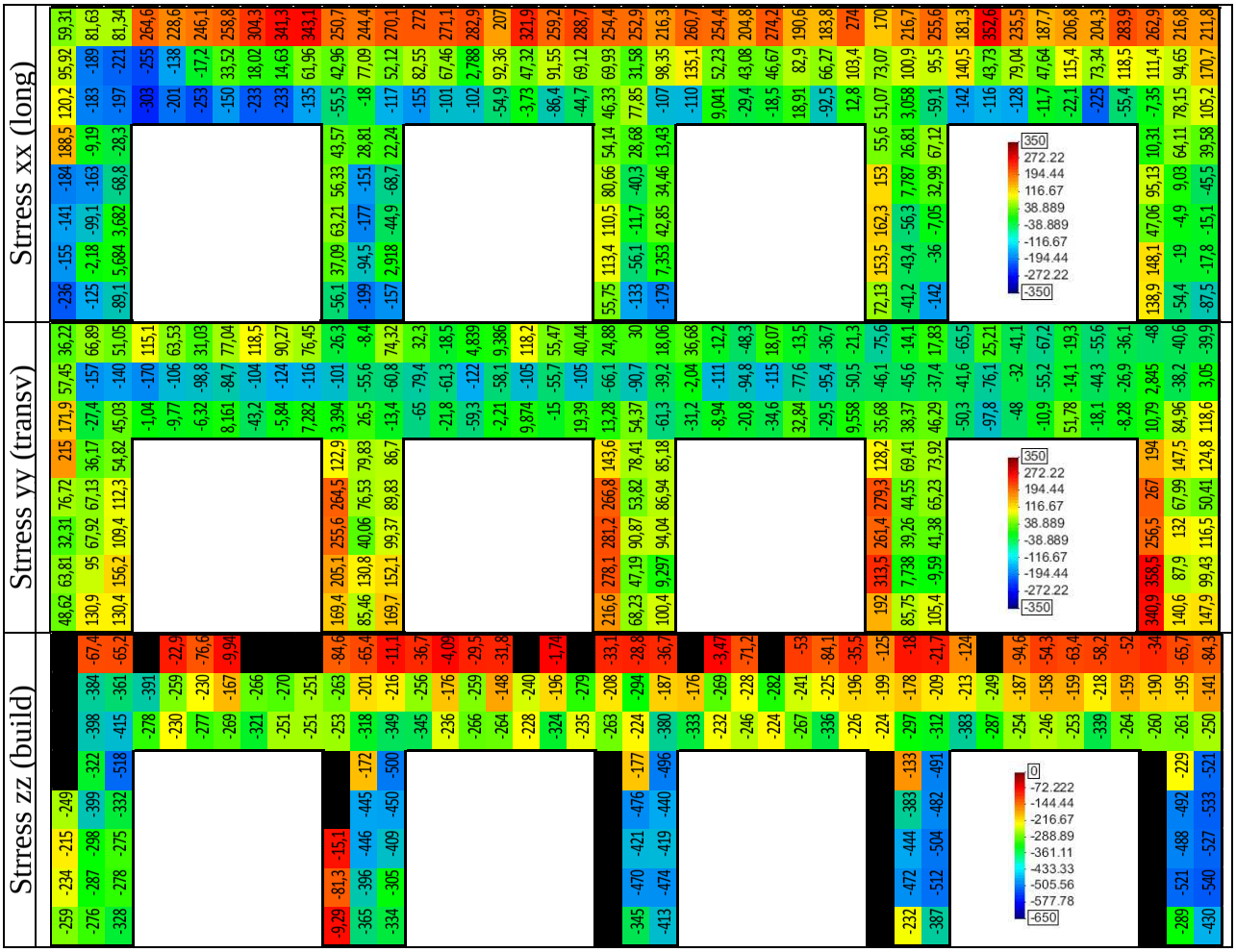

Figure 16: Result of residual stresses of the Benchmark study

Some highlights regarding the results are commented as follows. The stresses in *xx* direction are highly tensile at the upper part of the sample. Also, there is a noticeable compressive zone at the upper-left side of the sample and the stress behavior at the legs is mostly compressive, especially on the left ones. At the upper part of the sample, a noticeable gradient in the *zz* direction is shown.

The stresses in *yy* direction are more or less smooth at the upper part of the Cantilever and there are no gradients in *zz* direction like in the previous case. Also, high concentration of stresses is seen at the left part of the legs.

The stresses in *zz* direction are mainly compressive, with a high concentration in the legs, especially in the ones at the right. It is seen that the stresses values in the upper layers are the lowest. In average, it is shown that the values of the stresses in *zz* are the highest compared to the others axial directions.

5. Numerical Results and discussion

The intention of this section is to present the results of this research and explain the general workflow followed. To be able to test the "shrinkage" and "plastic" models, the suitable values of inherent strains were needed. In this sense, a simple prismatic geometry called "hatch" is used as sample to perform sensibility analysis of the parameters that define the inherent strains. This geometry was selected since it is small, making it easier to handle in terms of computational resources.

Once the optimal parameters are obtained, they are used in the Cantilever model to perform validation of the Inherent Strain Method. A summary of the previously explained workflow is shown in Figure 17 and the presentation of the results will follow this sequence.

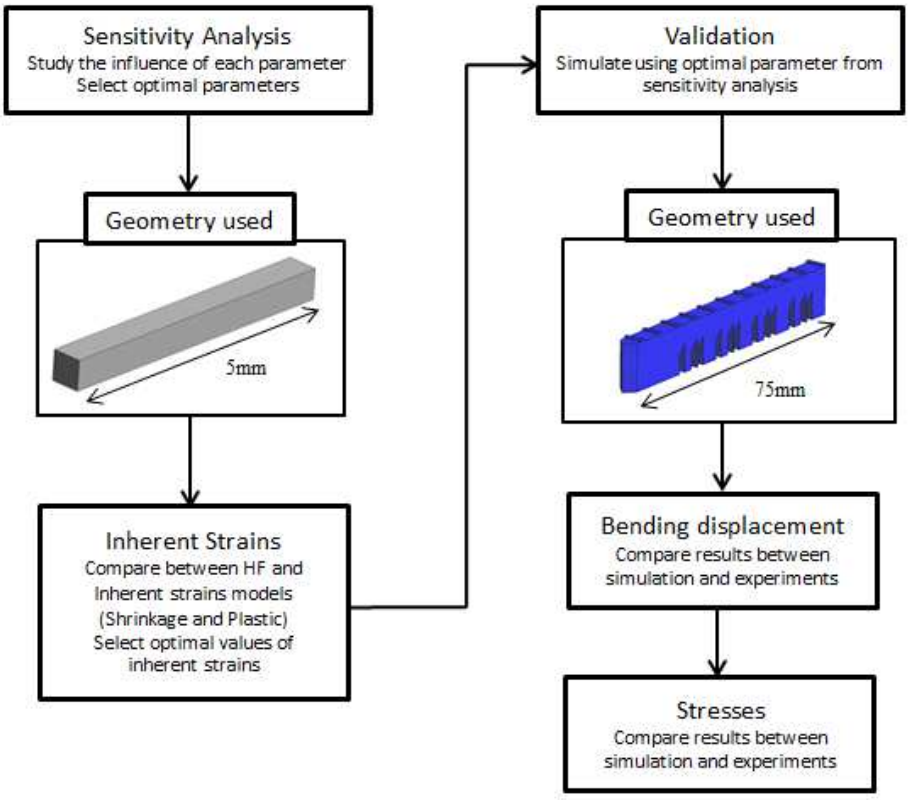

Figure 17: workflow of the present investigation

5.1. Inherent Strains selection

In this section, the results of the parameter selection for the inherent strains method are shown. The sensibility analysis of the user-defined parameter is performed using the hatch geometry (see Figure 18), which is used only for calibration purposes. It consists in a parallelogram of 0.5mm x 0.5mm x 5mm that simulates a layer height of 500µm, which is the value of layer height used in the validation model. The HF simulation is performed and used as reference for the selection of the parameters.

The same material from the Cantilever geometry (INC 625) is used, whose properties are summarized in Table 1 and Table 3. Regarding the material model of the simulations it must be highlighted that perfect plasticity behavior is assumed for the sake of simplification [21].

Table 3: Plastic properties of Inconel 625

Property	Value	Unit
Elastic limit	800	MPa
Isotropic Hardening Parameter	0	GPa

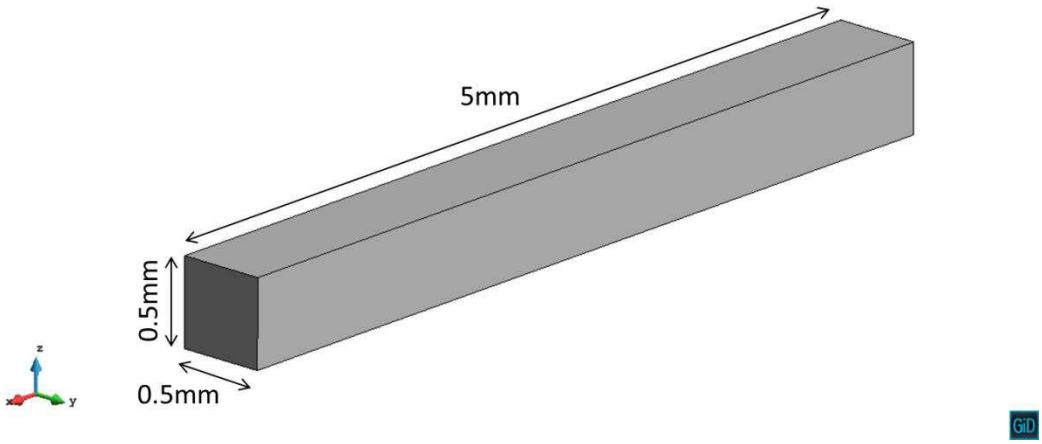

Figure 18: equivalent hatch used for models parameterization

Figure 19 shows the mesh used for the parameter's calibration and consists of structured, hexahedral, linear (8-noded) elements with size of 20µm in *z* and *y*, 25µm in *x*. This mesh represents the actual size of layer height and hatch and is used to perform High Fidelity simulation.

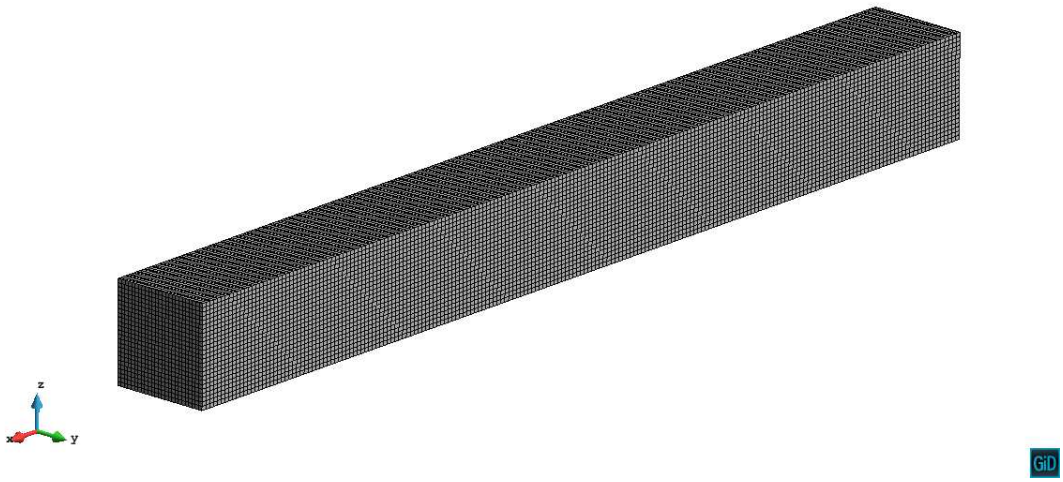

Figure 19: equivalent hatch meshed

The work done in the following section can be summarized as follows:

- Sensitivity analysis for Shrinkage model: in this step different values of the parameter T^{inh} of equation (42) are tested to see the impact on the stresses results. The main objective is to select the optimal parameter that gives the minimum difference when compared to the High fidelity model.
- Sensitivity analysis for Plastic model: Similarly to previous step, several values of the parameter T^{inh} and e^{inh} of equation (43) are tested to see the impact on the stresses. The main purpose is to select the optimal parameters that give the minimum difference when compared to the High fidelity results.

5.1.1. Sensitivity analysis of shrinkage model

In this section, the different values of inherent strains (parameterized by T^{inh}) are simulated to see the influence in the stresses results (sensitivity analysis) and be able to select a value suitable for validations. In this sense, 3 values (700, 800 and 900) of T^{inh} are tested. The one that gives a closer result to the reference (High Fidelity) is the one selected for the validation. The results in each axial direction are compared in points {x, 0.25mm, 0.25mm} (mid axle) and shown in Figure 20, Figure 21 and Figure 22. In each figure, 4 values are plotted: the results of the high fidelity model, and the results of the shrinkage model with the 3 different values of T^{inh}.

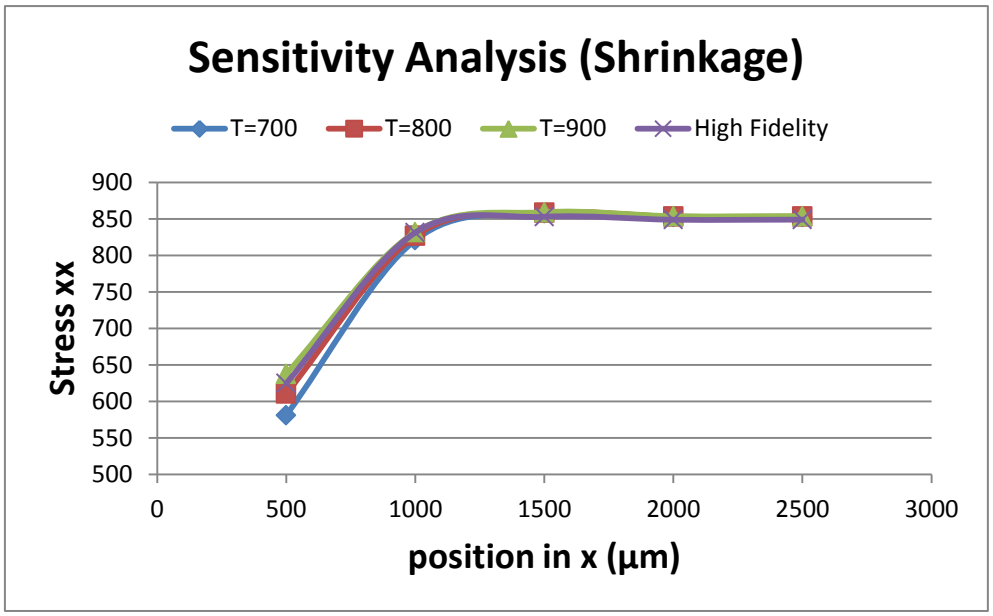

Figure 20: comparison of thermal inherent in xx (long) direction

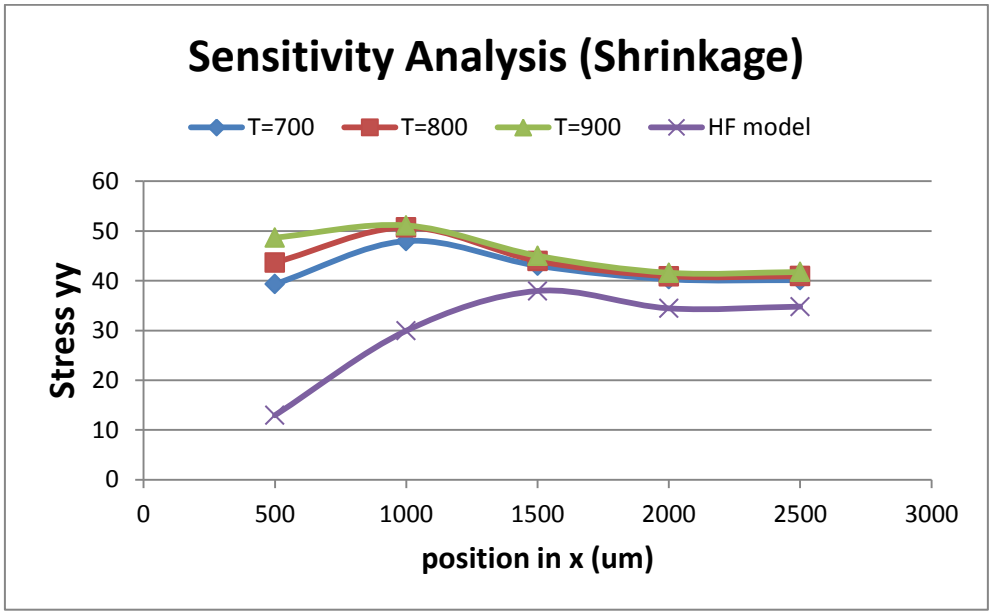

Figure 21: comparison of thermal inherent in yy (transverse) direction

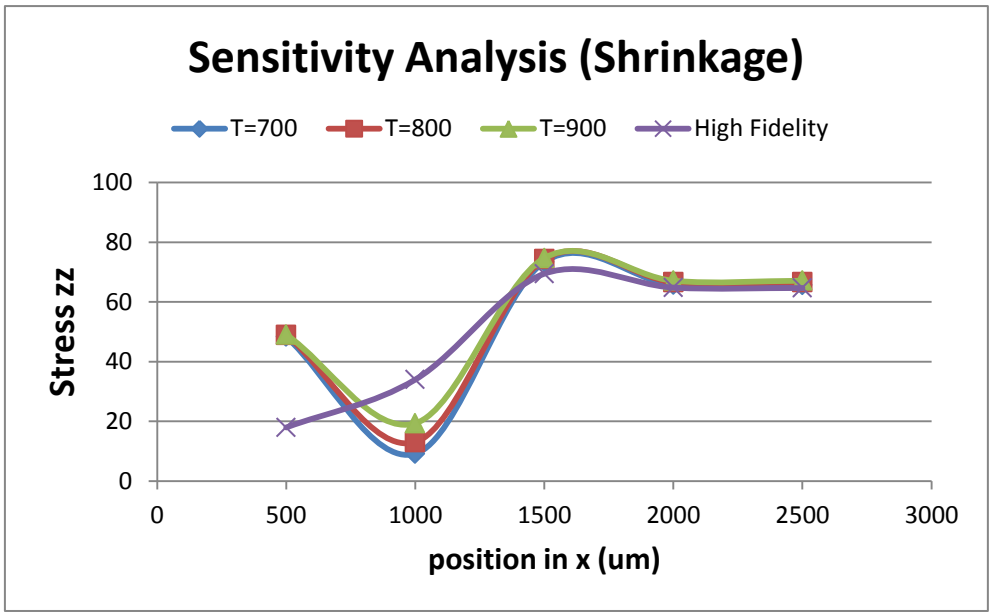

Figure 22: comparison of thermal inherent in zz (build) direction

The first observation of the sensitivity analysis is that the variations in stress values are very small for different values of thermal inherent strains, probably due to the perfect plasticity condition of the material. However, the differences are more noticeable at the boundaries of *x*. In *xx* direction, the values obtained are very close to the reference. On contrary, the values in *yy* and *zz* are not so accurate giving an error around 300% and 150% respectively. For S*yy* and S*zz* it can be seen that the results do not converge to the HF values and is not possible to achieve same accuracy in all directions, which suggests that non-isotropic inherent strains should be considered as a different approximation.

The value of *T*=800°C was selected since the stress values are closer to reference model at the borders of the hatch. This value gives an thermal deformation of 1,01E-2 when the HF model returns a value of 1,26E-2.

5.1.2. Sensitivity analysis of plastic model

In this section, the different values of inherent strains (parameterized by T^{inh} and e^{inh}) are simulated to see the influence in the stresses results (sensitivity analysis) and be able to select values suitable for validations. In this sense, a suitable value of e^{inh} was selected and 3 values (900, 1025, 1150) of T^{inh} are tested to see the influence in the results. The one that gives closer results to the reference (High Fidelity) is the one selected for the validation. The results in each axial direction are compared in points {x, 0.25mm, 0.25mm} (mid axle) and shown in Figure 24, Figure 25 and Figure 26. In each figure, 4 values are plotted: the results of the high fidelity model, and the results of the plastic model using 3 different values of T^{inh}.

To select the plastic inherent parameter e^{inh}, the value from HF model in *xx* direction was used, this value corresponds to 9E-3 as in can be seen in Figure 23.

Figure 23: Plastic Strain in xx direction

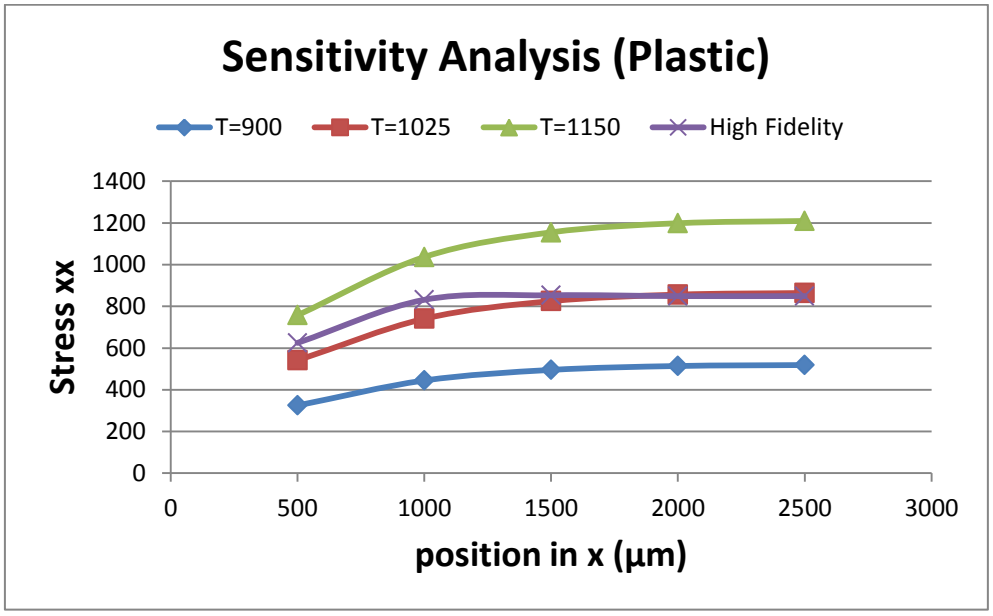

Figure 24: comparison of thermal inherent in xx (long) direction

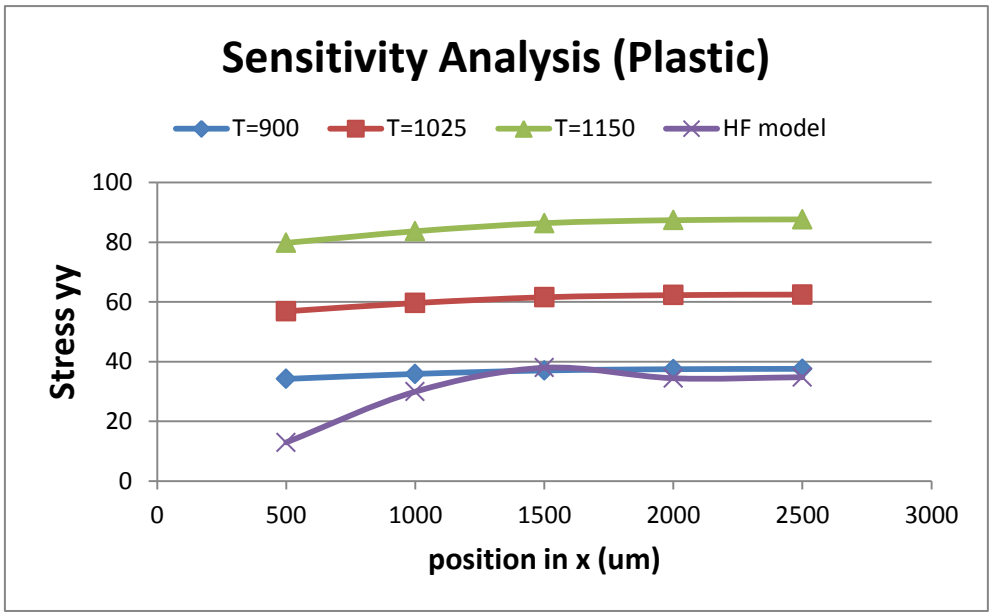

Figure 25: comparison of thermal inherent in yy (transverse) direction

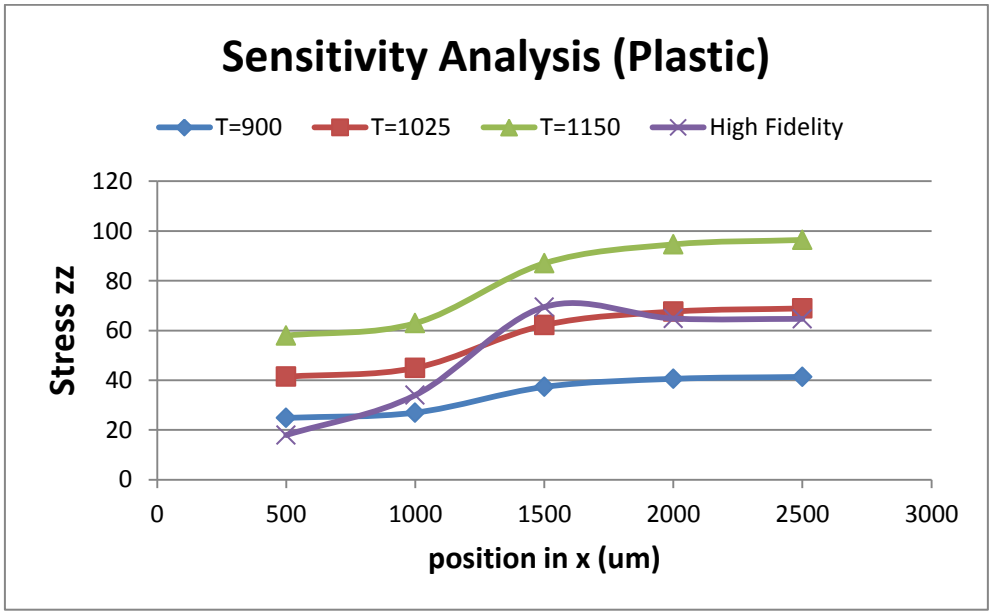

Figure 26: comparison of thermal inherent in zz (build) direction

In contrast to the shrinkage model, variations in stress are noticeable for different values of T^{inh}. For *xx* direction, the values obtained with T^{inh}=1025 are very close to the reference. Similarly as in the shrinkage model, in this model is not possible to achieve same accuracy in all directions, for example it is seen that for S*xx* and S*zz* the value with best fit is T^{inh}=1025 but for S*yy* the best is T^{inh}=900. This behavior suggests that different non-isotropic combination should be considered.

To select the final parameter of inherent strain, the value of L2-norm of the error is computed for each parameter and stress direction, and the one with the minimum average norm is used for the validation. The parameter selected is T^{inh}=1025, since L2-norm of the error was the minimum as it is shown in Table 4.

Table 4: L2 norm of error for each case of plastic strains sensitivity

	T=900	T=1025	T=1150
Sxx	768	128	634
Syy	22	70	124
Szz	48	27	68
AVG	**279**	**54**	**275**

After this analysis it is possible to select suitable user-defined parameters to define the inherent strains according to equations (42) and (43). The values selected are summarized in Table 5.

Table 5: Summary of the simulations and parameters used for validation

Sim	Model	User-defined parameters
1	Shrinkage	T^{inh}=800
2	Plastic	T^{inh}=1025, e^{inh}=9E-3

5.2. Validation with Cantilever geometry

After selecting the optimal parameters from sensitivity analysis, the next step is to perform the models validation. The layer-by-layer strategy is adopted to simplify computation time since other researchers have demonstrated that this simplification do not affect significantly the results [15]. Then, the results obtained in each simulation are compared with the given experimental data presented in section 4. The structure followed in this section is:

- Comparison of distortion values in build direction; between experiments and Inherent Strains models.
- Quantitative comparison of axial stresses between experiments and Inherent Strains models in line {x, 0, 8.072}.
- Results of Inherent Strains models and qualitative comparison of axial stresses in the X-Z mid-plane.

The mesh used for the numerical simulation of the Cantilever consists of unstructured, tetrahedral, linear (4-noded) elements with global size 300μm. Figure 27 and Figure 28 show the mesh on the Cantilever geometry. Due to computational limitation, this is the finest size that was possible to simulate with this geometry. The Cantilever geometry consists of 1.4 million elements. The material properties used in this simulation are the one specified in Table 1 and Table 3 corresponding to super-alloy Inconel 625.

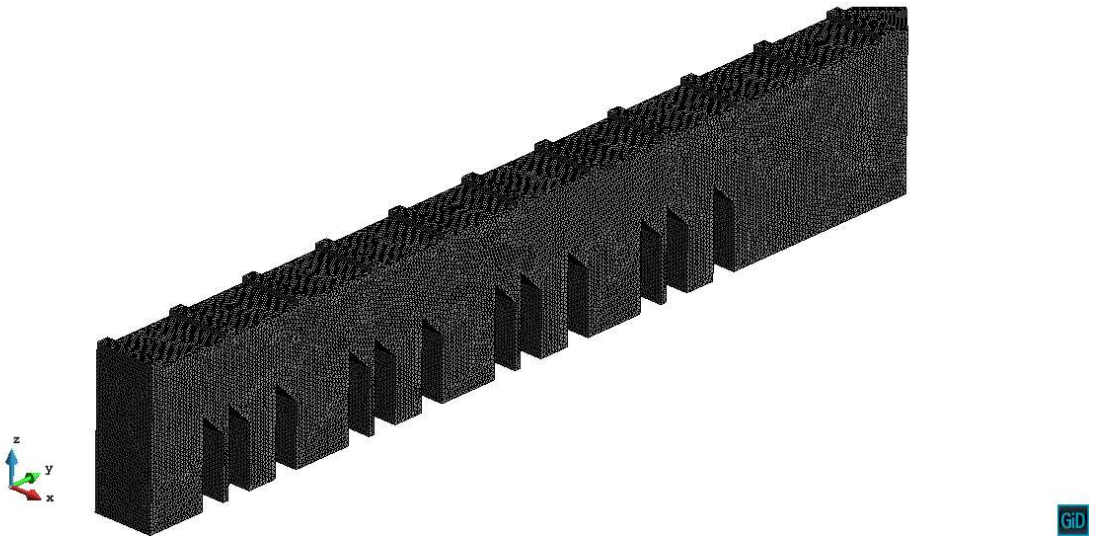

Figure 27: cantilever meshed with mesh 2. Total of 1.4 million elements

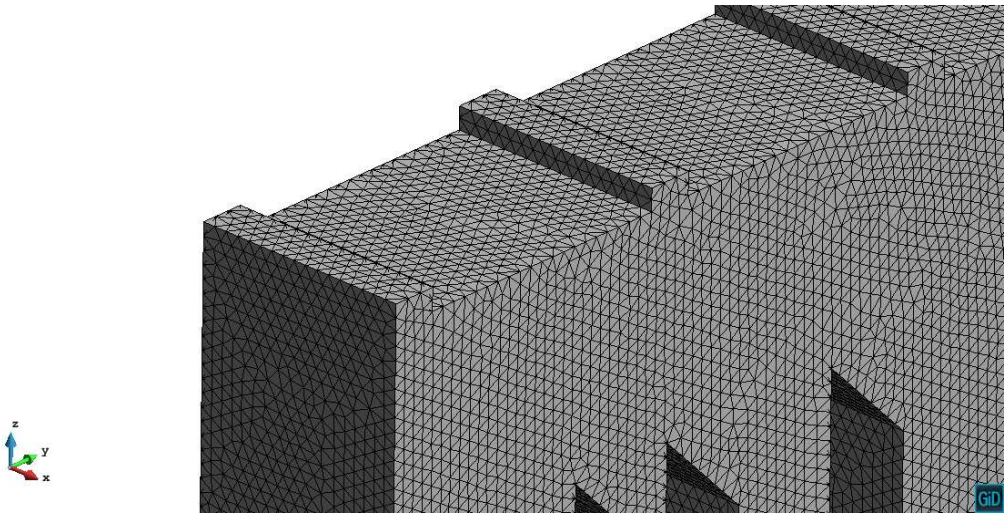

Figure 28: zoom of Figure 27

5.2.1. Distortions

In this section, the values of the vertical distortions after cutting the sample legs are obtained from the benchmark. The experimental values are compared with the numerical results obtained from the simulation 1 (shrinkage) and 2 (plastic) and are plotted in Figure 29. Also, the error estimation is made for the displacements and the values are plotted in Figure 30 to assess the accuracy of the models in terms of displacements.

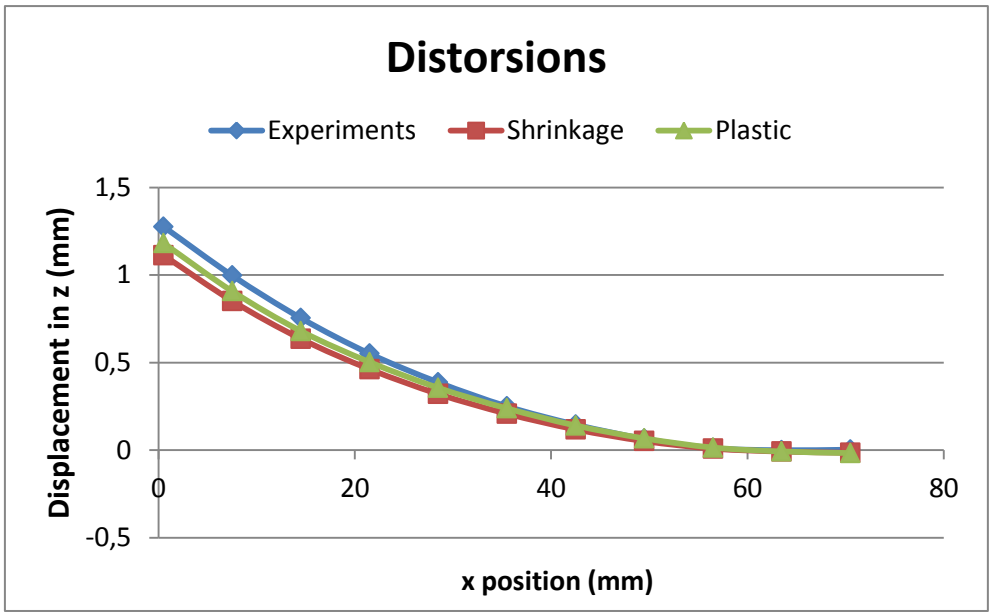

Figure 29: displacements comparison

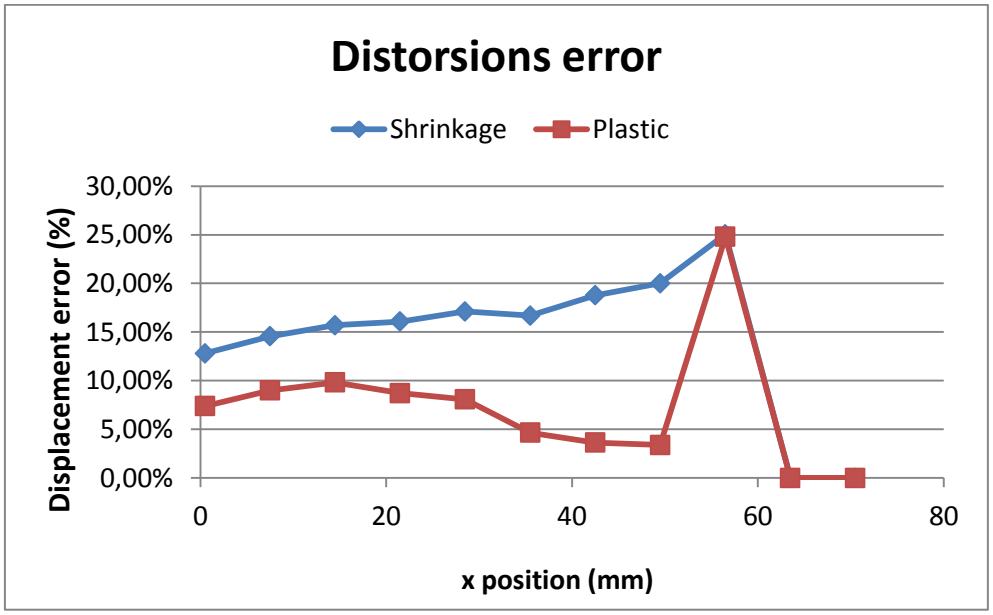

Figure 30: displacements error between models

It is seen that the displacement error is lower for the Plastic model comparing to the Shrinkage one. However, this result can be improved by developing a more robust way to obtain the parameters from calibration geometry, possibly using a different and more representative geometry. It is seen that despite the mesh size, it is possible to obtain more or less accurate results, especially for "Plastic" model.

5.2.2. Quantitative comparison of stresses in axial directions

In this section, the experimental values of the axial residual stresses before cutting the sample legs are compared with the numerical values obtained from the simulation 1 (shrinkage) and 2 (plastic) and the results are plotted in Figure 31, Figure 32 and Figure 33 (one figure for each direction). A random sampling of points at Y=0 and Z=8,072mm are selected to make

the qualitative comparison. The values of the stresses are computed from the values of the residual strains obtained from the benchmark study mentioned in section 4.2.

Also, the error estimation is made to quantify the accuracy of each model. The error plot from the Shrinkage model is shown in Figure 34 and analogous plot for the Plastic model is shown in Figure 35.

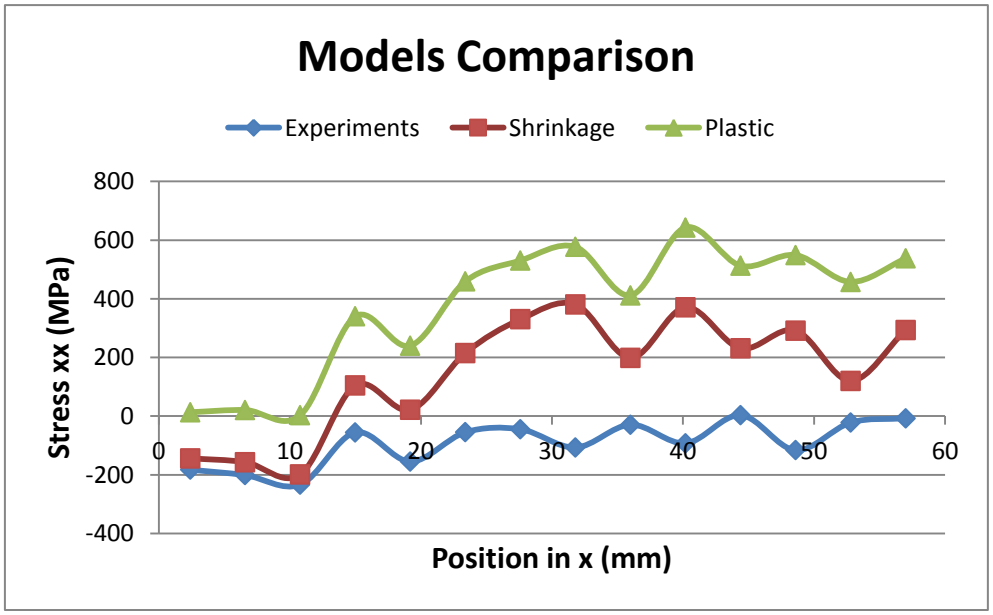

Figure 31: stresses comparison between models in xx (long) direction

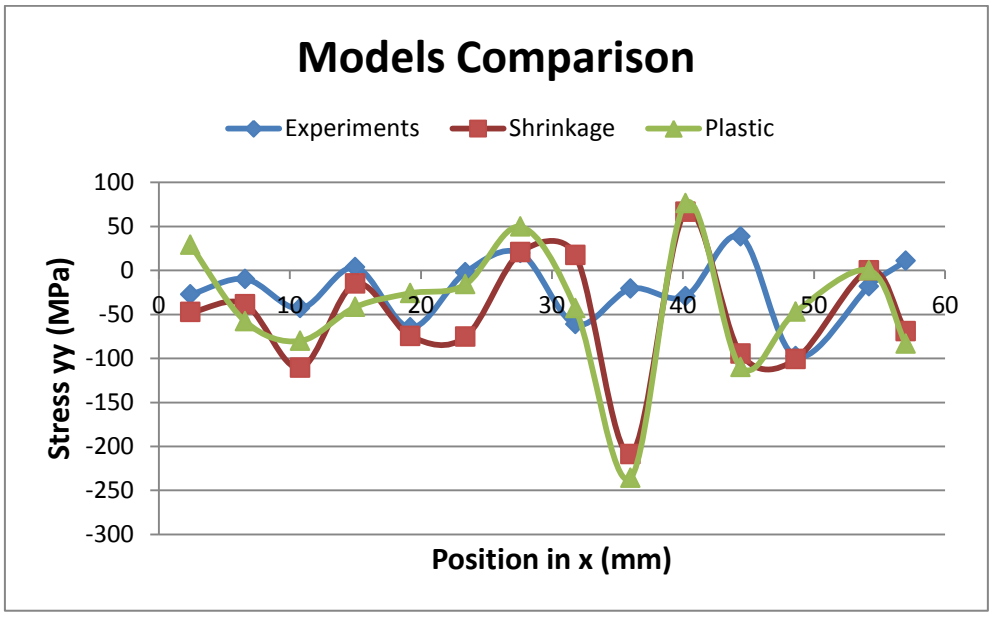

Figure 32: stresses comparison between models in yy (trans) direction

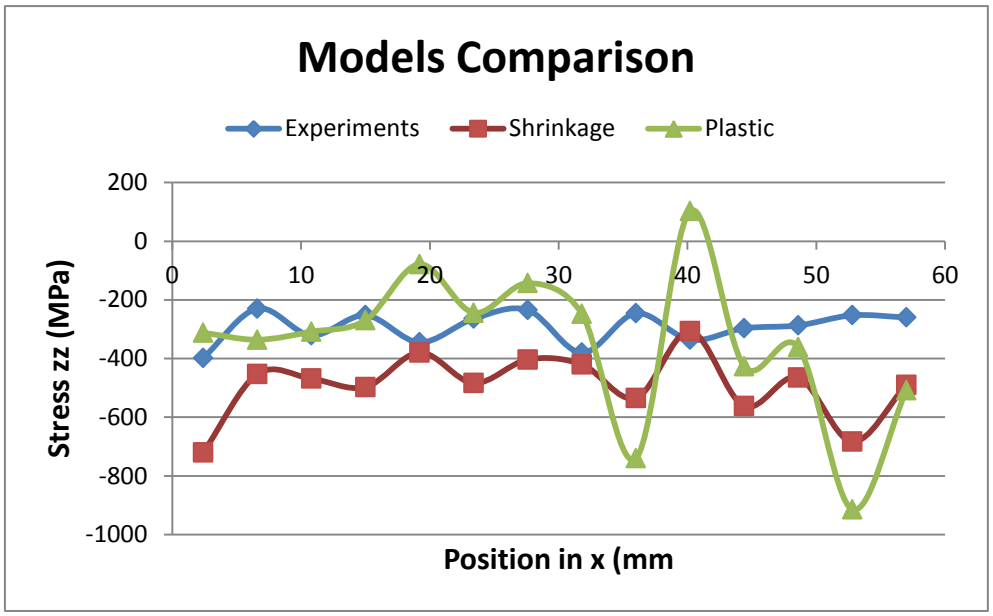

Figure 33: stresses comparison between models in zz (build) direction

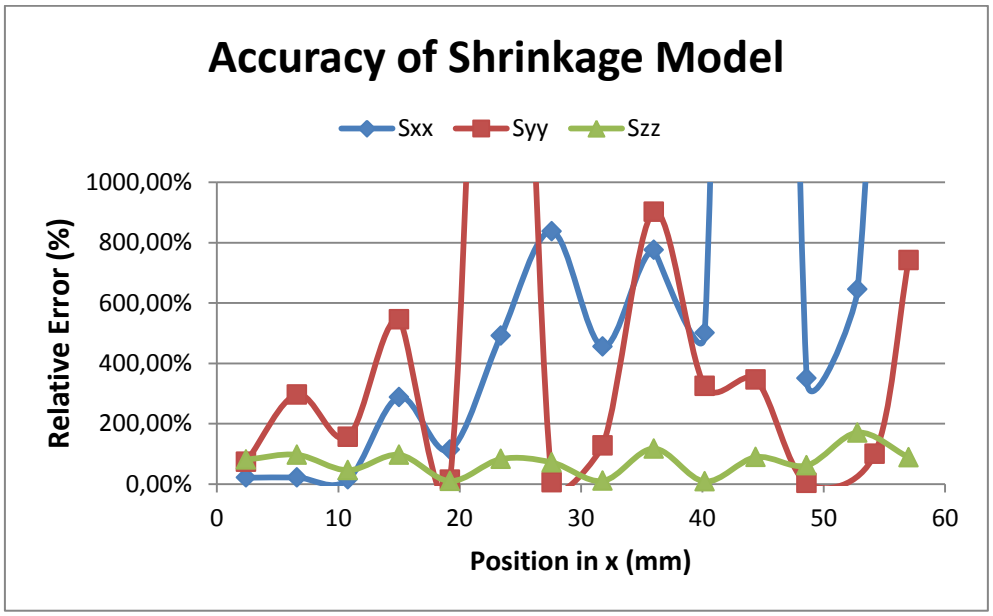

Figure 34: Accuracy of the Shrinkage Model

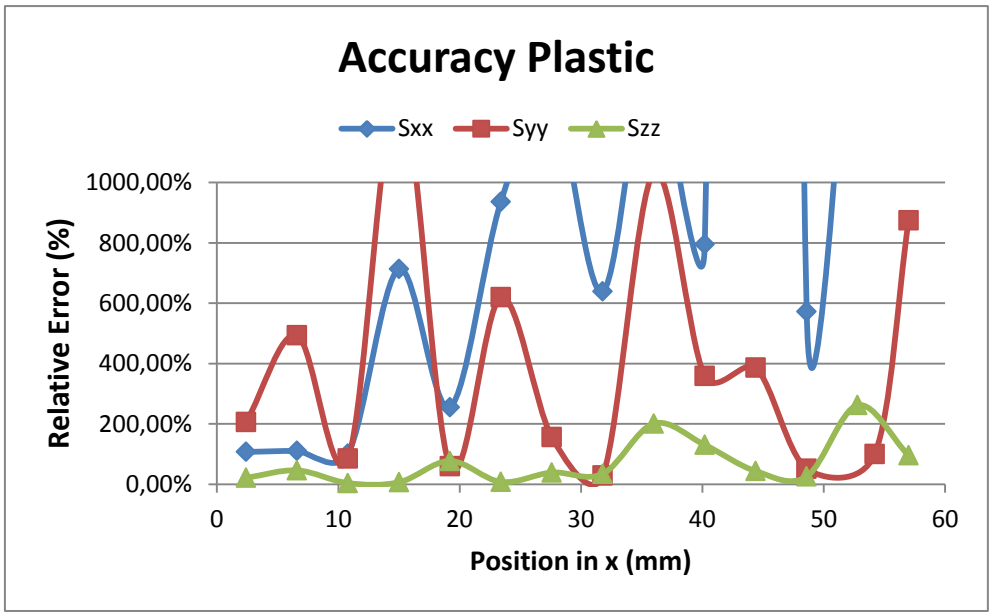

Figure 35: Accuracy of Plastic Model

In general, it is observed that in both simulations and experiments the results are not smooth with respect to *xx* direction. Oscillation and alternative gradients are present along this direction and it is not clear if this behavior is natural from the problem or is related to measurements accuracy. It is seen in Figure 31 that stresses values are higher for the plastic model comparing to the shrinkage model and to the experiments.

It is seen that the results of the simulations are not accurate since errors larger than 100%. However, with Figure 34 and Figure 35 is possible to see that in both shrinkage and plastic models, the error in *zz* is significantly lower comparing to *xx* and *yy* directions. It is highly suspected that the mesh size has a big influence in these results since this kind of problems have a very local behavior that the used mesh was not able to catch.

As a remark, at Z=8.072mm the values of stresses in *zz* are mainly compressive and the numerical model was able to reproduce this qualitatively. In *xx* and *yy* direction the stresses oscillations are close to zero and there is a significant difference between experiments and numerical results.

It is seen also that the values of stresses from inherent strains models are higher comparing to experimental data. This is probably due to the way the inherent strains are being applied, since it is done in one mechanical step instead of being applied smoothly in more steps. This could have an impact in the way the residual stresses are developed.

5.2.3. Qualitative comparison of stresses in the axial directions

For the qualitative comparison, a color map of stresses at mid-plane *Y*=0 is obtained to compare the result between the *shrinkage* model, the *plastic* model and the experiments. The idea of this section is to compare stress values qualitatively to assess if the models are able to reproduce the actual stress distribution. Figure 36, Figure 37 and Figure 38 show the comparison of stress distribution on the longitudinal, transversal and build direction of the numerical models, respectively.

Stress in xx (longitudinal)

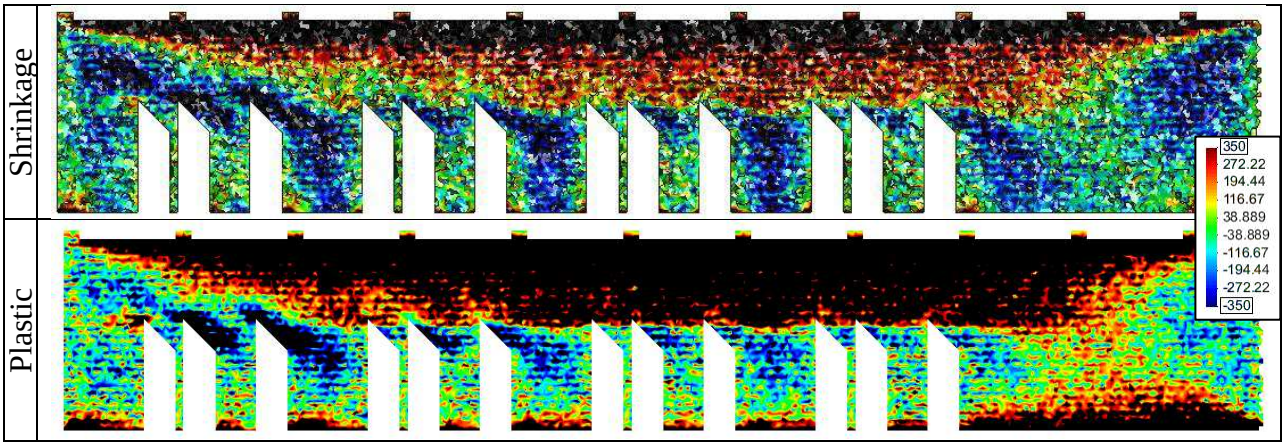

Figure 36: Comparison of stresses in xx (long) direction of all models

It is seen that in the upper left region of the Cantilever, there is a zone of compressive stress that is present in both simulations and experiments. However, this compressive zone is more noticeable in the shrinkage model.

In the simulation is it seen that the upper part of the geometry is dominated by tensile stresses, which agrees with the experiments, however the gradients are very different. It is seen that the values in the simulations are higher, and they concentrate in the upper middle zone, especially in the plastic model.

In the simulation, all legs seem to have high compressive stresses at the center of the structure. This result is not seen in the experiments, except for the leg of the left. In general it is seen that the stress distribution of the simulations do not completely agree with the distribution of the experiments. Also, it must be remarked that in the plastic model the values of stresses are higher comparing to shrinkage one.

Stress in yy (transversal):

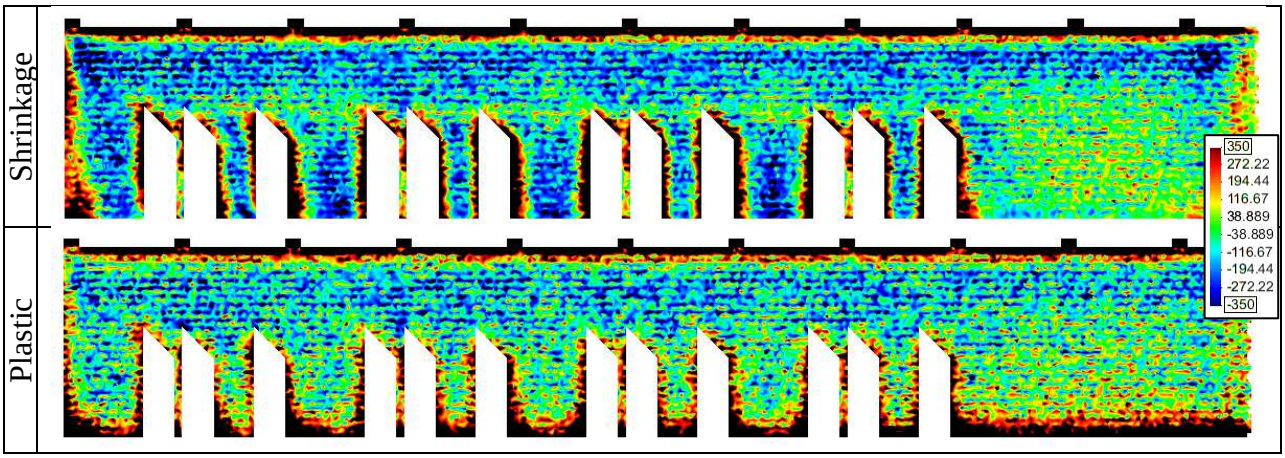

Figure 37: Comparison of stresses in yy (trans) direction of all models

In the shrinkage simulation, a thin layer of the upper region is under compressive stress, but in the experiments this region is thicker and the values of the stresses are lower. Also, the

values of stresses within the legs in the plastic model are slightly tensile as in the experiments. However, this behavior does not happen in the shrinkage model.

In the experiments and the simulations it is seen that the left and right parts of the legs are subjected to compression. However, in the experiments it can be appreciated that the left part is more tensed than the right part. But, for the simulations left and right parts seems to have a symmetric pattern.

The stress distribution of the plastic model is similar to the experimental distribution, since compressive behavior at the upper region and tensile behavior at the legs is present in both. Then, it can be said that the plastic model and the experiments have qualitatively the same stress distribution.

However, in the shrinkage model the legs are subjected to compressive stresses, on the contrary when compared to the plastic model. Also, similarly as it happens with S*xx*, the values of stresses are higher in plastic model with respect to shrinkage model.

Stress in zz (build):

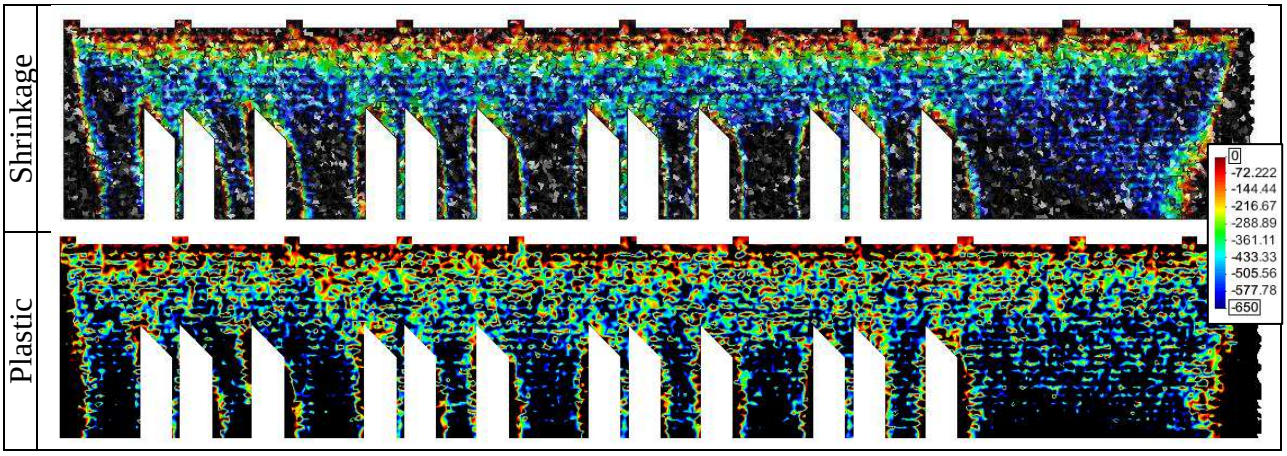

Figure 38: Comparison of stresses in zz (build) direction of all models

The first remark is the presence of the high compressive region in both simulations and experiments at the Cantilever legs. In this case the stress distribution of experiments and simulations are very similar between each other. Also, the stress gradient in *zz* is similar between experiment and simulations, in both cases the lowest values are at the upper region and the highest values are at the lowest region of the sample.

In general, qualitative analysis shows that stress behavior in *xx* direction do not comply with the experiments, in the *yy* direction the results of plastic model comply with the experiments and in the *zz* direction the stress distribution is very similar comparing to experiments. As a final remark, the values obtained from all simulations are higher comparing to the ones obtained in the experiments.

6. Identification of source of errors

The idea of this section is to identify the possible sources of error arisen from the simplifications made in the validations model. For this purpose, the hatch geometry is used to be able to compare with the HF model and obtain results quickly. Table 6 summarizes all simulations performed for this objective. Sim 3 represents the reference simulation, since it is performed with a highly refined mesh, the actual laser spot size, the actual layer size and using a hatch-by-hatch strategy. Then, the intention of Sim 4 is to see how the results get distorted when the layers are lumped with a ratio of 25:1 and when the layer-by-layer strategy is adopted. With Sim 5, the objective is to assess the impact of using a mesh of the size of the mesh used in the Cantilever validation sample. Then, with Sim 6 and 7 the objective is to assess the numerical errors introduced by using the inherent strains method. The final outcome from this section is to be able to identify which is the parameter selection that gives the worst result by analyzing the numerical error that each simplification introduces to a simple geometry.

Table 6: Summary of the simulations and parameters used for calibration

Sim	Model	MD layer	hatch	Mesh	Comments
3	High Fidelity	20μm	100μm	Structured, hexahedral, 20μm	Reference model
4	High Fidelity	500μm	500μm	Structured, hexahedral, 20μm	Layer by layer and lumped layers
5	High Fidelity	500μm	500μm	Unstructured, tetrahedral, 300μm	Cantilever mesh
6	Shrinkage	500μm	500μm	Structured, hexahedral, 20μm	T^{inh}=800
7	Plastic	500μm	500μm	Structured, hexahedral, 20μm	T^{inh}=1025, e^{inh}=9E-3

To compute the error plot, the values of stresses are taken from the mid-axle similarly as it was done in section 5.1 and the error calculation is done taking the HF as the reference value. Figure 39, Figure 40 and Figure 41 show the comparison in longitudinal, transverse and build direction respectively.

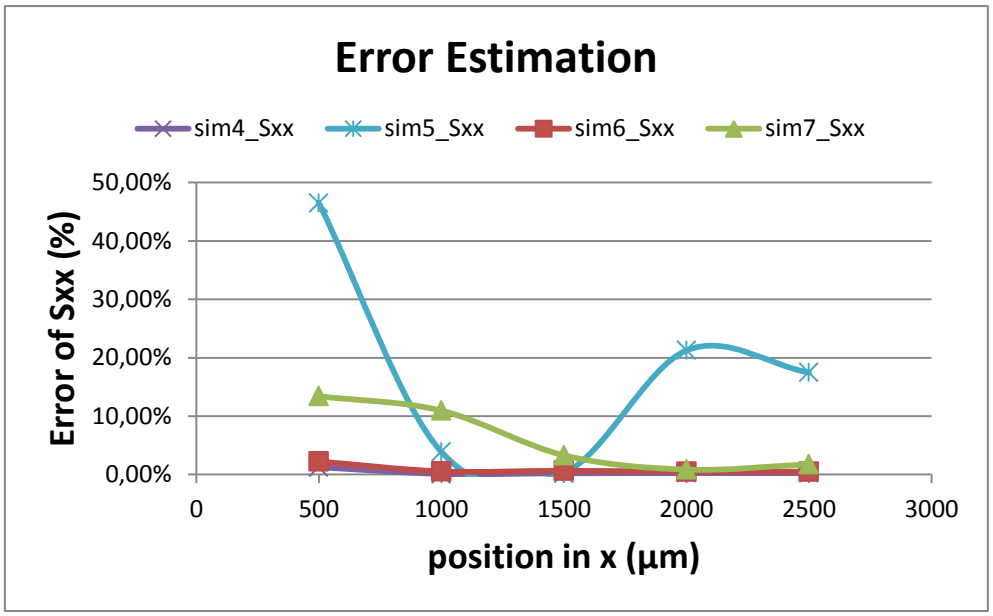

Figure 39: error estimation in xx (long) direction

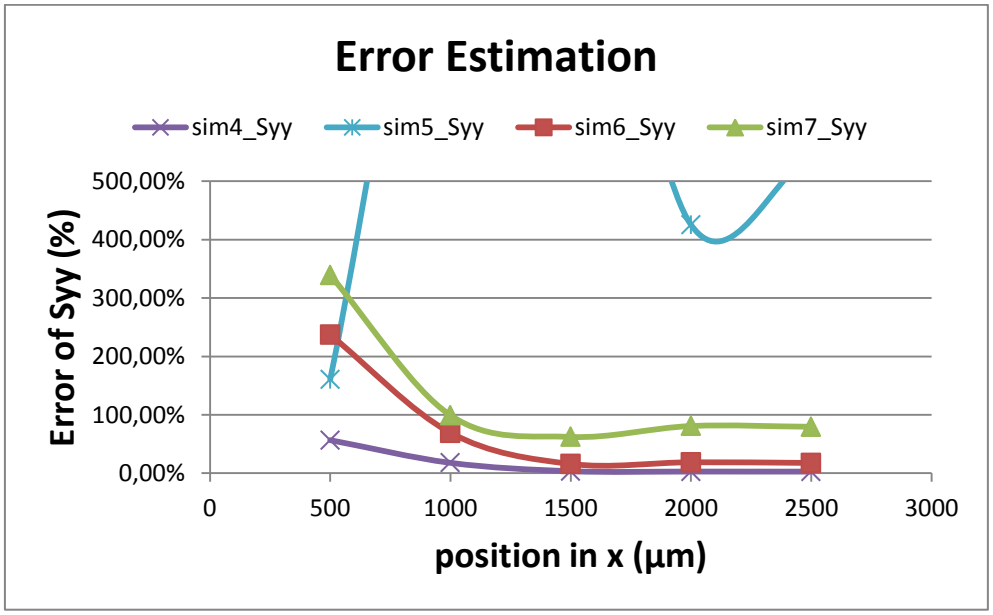

Figure 40: error estimation in yy (trans) direction

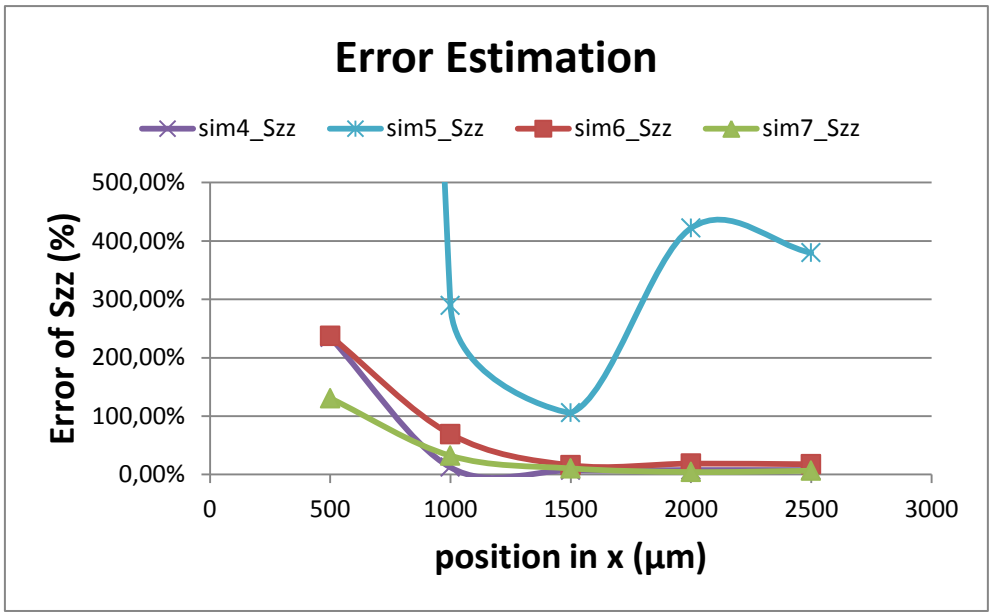

Figure 41: error estimation in zz (build) direction

One of the most noticeable aspects in these results is the high value of the errors in general, especially in the region close to x=0. It is seen that in all directions the highest error is obtained in Sim 5, which corresponds to the simulation using the mesh for the Cantilever model. It is seen that, the simplification done with the inherent strains method also has an influence in the accuracy that is not negligible.

However, from this analysis it can be concluded that special care must be taken to the mesh size. Despite the mesh size is very small with respect to the Cantilever model size; the physics associated with the SLM process involves a very local behavior that is not possible to reproduce using a mesh size of 300µm. In this sense, it cannot be concluded that the inaccuracy of this study is due to the inherent strain simplification since the mesh size has a big influence in the results as it was seen in the previous analysis.

7. Final conclusions

It is seen that the results in the validation are not accurate in terms of stresses, nevertheless for the displacement is possible to get results more or less accurate (around 10-15%). This suggests that the inherent strain method is capable of predicting deformations but not stresses. Also, the values of stresses obtained with the simulations are general higher comparing to the experiments.

Despite the results, the Inherent Strains Method shouldn't be discarded since it was demonstrated that the mesh size also has a big influence in these results. Then, another mesh strategy must be developed to be able to neglect the influence of the mesh size in the results. Another possible source of error is the way inherent strains are applied, since they are applied in one mechanical step instead of being applied smoothly. This problem is related to the high values of stress obtained from the simulations.

It has been shown that the inherent strains has not necessarily to be same in each direction, since if in one direction is calibrated in the other 2 doesn't match with the reference values. In this sense, an-isotropic values must be tested to see the influence in the results and if it is possible to obtain an improvement.

Qualitatively speaking, the patterns of the results of stress field in *zz* comply between simulations and experiments, despite values are higher in the simulations. In Stress field *yy* the pattern comply only with the plastic model. And for Stress field *xx* there are few similitudes between the simulation and the experiments.

It is seen that experimental values of stresses have an oscillating pattern along longitudinal direction. It is suspected that this behavior is due the high variation of stress within the gauge volume of 1.5mm, as consequence of the highly local heat-cooling cycles and when using a mesh size of 300μm is not possible to catch this behavior. However, this oscillating pattern is reproduced in the simulations but with higher amplitudes.

8. Proposals

After performing this work, several proposals are presented based on the investigation performed and the results obtained.

- Use domain decomposition to segregate high gradient volume (upper layers) with low gradient volume (lower layers). This way would be possible not only to use mismatching meshes but also cut the problem in blocks, using different mesh sizes in each block and opening the possibility to solve it by using parallel computing. That way the effect of the mesh size can be isolated.
- Change the way inherent strains are applied which currently is done in 1 mechanical step. It is done this way since at the beginning of the project it was thought that the important parameter is the final value, and the way it is applied is not relevant. However after some test with simpler geometries it shows that the way the inherent strains are applied affects the results of the stresses.
- Automate inherent strains selection with hatch or test geometry. Instead of performing visual analysis, create an algorithm that automatically selects the best parameter using the suitable test geometry.
- Use higher order elements for coarse mesh. In this case was not possible since is not implemented in the program.
- Another test geometry should be proposed, one that can match better the results errors between this geometry and the validation geometry.

9. References

[1] Industrial-laser, "Selective Laser Melting," 2016. [Online]. Available: https://www.industrial-lasers.com/articles/2016/03/selective-laser-melting-method-works-with-magnesium-alloys.html.

[2] L. Columbus, "The State Of 3D Printing, 2017," *Forbes*, 2017. [Online]. Available: https://www.forbes.com/sites/louiscolumbus/2017/05/23/the-state-of-3d-printing-2017/#721453b357eb.

[3] M. Chiumenti *et al.*, "Numerical Modelling and Experimental Validation in Selective Laser Melting," vol. 18, pp. 171–185, 2017.

[4] M. Chiumenti, M. Cervera, N. Dialami, B. Wu, L. Jinwei, and C. Agelet de Saracibar, "Numerical modeling of the electron beam welding and its experimental validation," *Finite Elem. Anal. Des.*, vol. 121, pp. 118–133, 2016.

[5] M. Chiumenti, X. Lin, M. Cervera, W. Lei, Y. Zheng, and W. Huang, "Numerical simulation and experimental calibration of additive manufacturing by blown powder technology. Part I: thermal analysis," *Rapid Prototyp. J.*, vol. 23, no. 2, pp. 448–463, Mar. 2017.

[6] L. Parry, I. A. Ashcroft, and R. D. Wildman, "Understanding the effect of laser scan strategy on residual stress in selective laser melting through thermo-mechanical simulation," *Addit. Manuf.*, vol. 12, pp. 1–15, 2016.

[7] G. Vastola, G. Zhang, Q. X. Pei, and Y. Zhang, "Additive ing Controlling of Residual Stress in Additive Manufacturing of Ti6Al4V by Finite Element Modeling," *Addit. Manuf.*, vol. 0, pp. 1–16, 2015.

[8] C. Li, J. F. Liu, and Y. B. Guo, "Prediction of Residual Stress and Part Distortion in Selective Laser Melting," *Procedia CIRP*, vol. 45, pp. 171–174, 2016.

[9] Y. Liu, Y. Yang, and D. Wang, "A study on the residual stress during selective laser melting (SLM) of metallic powder," *Int. J. Adv. Manuf. Technol.*, pp. 1–10, 2016.

[10] M. F. Zaeh and G. Branner, "Investigations on residual stresses and deformations in selective laser melting," *Prod. Eng.*, vol. 4, no. 1, pp. 35–45, 2010.

[11] C. Casavola, S. L. Campanelli, and C. Pappalettere, "Experimental analysis of residual stresses in the selective laser melting process," *Proccedings XIth Int. Congr. Expo. Orlando, Florida, USA*, no. January, 2008.

[12] J.-P. Kruth, J. Deckers, E. Yasa, and R. Wauthlé, "Assessing and comparing influencing factors of residual stresses in selective laser melting using a novel analysis method," *Proc. Inst. Mech. Eng. Part B J. Eng. Manuf.*, vol. 226, no. 6, pp. 980–991, Mar. 2012.

[13] J. Saarimäki, M. Lundberg, and J. J. Moverare, "3D Residual Stresses in Selective Laser Melted Hastelloy X," vol. 2, pp. 73–78, 2017.

[14] H. Ali, L. Ma, H. Ghadbeigi, and K. Mumtaz, "In-situ residual stress reduction, martensitic decomposition and mechanical properties enhancement through high

temperature powder bed pre-heating of Selective Laser Melted Ti6Al4V," *Mater. Sci. Eng. A*, vol. 695, pp. 211–220, 2017.

[15] P. Alvarez, J. Ecenarro, I. Setien, M. S. Sebastian, A. Echeverria, and L. Eciolaza, "Computationally efficient distortion prediction in Powder Bed Fusion Additive Manufacturing," *Int. J. Eng. Res. Sci.*, vol. 2, no. 10, pp. 2395–6992, 2016.

[16] N. Ma *et al.*, "Inherent Strain Method for Residual Stress Measurement and Welding Distortion Prediction," *Vol. 9 Prof. Norman Jones Honor. Symp. Impact Eng. Prof. Yukio Ueda Honor. Symp. Idealized Nonlinear Mech. Weld. Strength Struct.*, no. January 2017, p. V009T13A001, 2016.

[17] A. Escobar, D. Celentano, M. Cruchaga, and B. Schulz, "On the Effect of Pouring Temperature on Spheroidal Graphite Cast Iron Solidification," *Metals (Basel).*, vol. 5, no. 2, pp. 628–647, 2015.

[18] Y. UEDA, H. MURAKAWA, K. NAKACHO, and N. Ma, *Establishment of Computational Welding Mechanics(Mechanics, Strength & Structural Design)*. 1995.

[19] N. Keller and V. Ploshikhin, "New Method for Fast Predictions of Residual Stress and Distortions of AM Parts," *Solid Free. Fabr. Symp.*, pp. 1229–1237, 2014.

[20] NIST, "BENCHMARK TEST DATA," *NIST*, 2018. [Online]. Available: https://www.nist.gov/ambench/benchmark-test-data. [Accessed: 01-Jul-2018].

[21] C. C. Clickner *et al.*, "Mechanical properties of pure Ni and Ni-alloy substrate materials for Y-Ba-Cu-O coated superconductors," *Cryogenics (Guildf).*, vol. 46, no. 6, pp. 432–438, 2006.